PD-EAD/2014/1003

Effect of MAV configuration on flow and performance

MUKUND R, CHANDAN KUMAR A
Experimental Aerodynamics Division

PD-EAD/2014/1003
August 2014

ISO 9001: 2008
CERTIFIED

वैज्ञानिक तथा औद्योगिक अनुसंधान परिषद्
Council of Scientific & Industrial Research
राष्ट्रीय वांतरिक्ष प्रयोगशालाएं
National Aerospace Laboratories
बेंगलूर/ Bangalore-560 017, भारत/ India

Contents

Effect of MAV configuration on flow and performance

R Mukund and A Chandan Kumar

Experimental Aerodynamics Division, NAL, Bangalore

Abstract

Systematic experimental studies were taken up in the 1.5m wind tunnel at NAL on thin constant-thickness MAV planforms to study the effect of a variety of planform configurations on the flow and MAV performance.

The first phase was a configuration study over a variety of MAV planform shapes and camber conducting force and pressure measurements along with surface oil flow visualization. In the present second phase, selected planforms were used to study different aspects of the configuration like powered propellers, the leading edge shape and planform aspect ratio. PIV studies on the MAV planform conducted to study the leading edge bubble, the tip vortices and their interactions are reported in the third phase.

Nomenclature

c - planform chord at mid span location, m

C_A - Coefficient of axial force

C_D - Coefficient of drag

C_L - Coefficient of lift

C_M - Coefficient of pitching moment about the quarter chord

C_N - Coefficient of the normal force

C_p - Coefficient of pressure

L/D - Lift to drag ratio

Re - Reynolds number based on the chord and the freestream velocity

V - Freestream velocity, m/s

x - Streamwise distance from the leading edge, m

x_{RA} - distance x to reattachment

α - Angle of attack, deg.

1. Introduction

Micro Aerial Vehicles (MAV) are being developed all round the world for a variety of civilian and military purposes. One of the configurations being developed at NAL is a fixed wing MAV of 300mm size weighing nearly 300gm capable of flying for 20-30 minutes in autonomous flight, with payload. The aerodynamics of such MAVs having restricted span and flying at low Reynolds numbers is much different from that of a typical aircraft [1-3]. These MAVs have a near circular wing planforms similar to the ones designed by Zimmermann [4] and have a sharp leading edge and thin cambered sheet instead of a thick airfoil. Several such MAVs have been designed and successfully flown all over, however the flow over the MAVs wing is not well

understood, especially the mechanism of obtaining lift at high incidences. Further, established design procedures for conventional aircrafts may not be applicable for MAV design. Computation of such complicated low Reynolds number flows is rather difficult. Thus experimental studies are of utmost importance for not only understanding the flow but also for optimizing the design.

The first phase of experiments consisted of the characterization of a variety of MAV planform shapes and camberline distributions in the 1.5m low speed wind tunnel at NAL and reported in [6] and summarized in the next section.

Presently, further experiments have been conducted on chosen planforms to understand the flow over MAV planforms with the following objectives –

- Conduct pressure measurements on a chosen planform at different angles of attack and freestream velocity.
- Study the effect of rounding the leading edge with force measurements and flow visualization.
- Study effect of planforms with two aspect ratios.
- Assess the effect of propeller on MAV performance.

2. A review of previous work

The last two decades have seen a wide spread research in the field of MAVs and Low Reynolds number aerodynamics. The understanding of the flow field in the high Reynolds number regime, the development of appropriate computational techniques/codes and the design methodologies of airfoils/wings/aircrafts are very well developed. However, the low Reynolds number regime, in which the MAV generally operate, poses interesting challenges towards airfoil design. Reviews by Carmichael [1], Lissaman [2], Mueller [3] and Stanford [6] reveal that the flow at the low Reynolds numbers applicable to MAVs ($5x10^4$ to $20x10^4$) is much different from that of a typical aircraft we are used to. In this range of Reynolds numbers, the boundary layer remains laminar and is very much susceptible to separation at high incidence, badly affecting its performance. If the Reynolds number is increased, the separated shear layer undergoes transition to turbulence, in effect causing the reattach of the boundary layer forming the so called laminar separation bubble (LSB). The separation, the bubble formation and its bursting can have a significant effect on the performance especially in degrading it and increasing its uncertainty.

The MAVs are generally designed with restricted wing span reducing the aspect ratio of the wing planform to near unity or less. This constraint has resulted in efforts to maximize the area available for lift generation a popular example is the combination of two semi-ellipses by Zimmermann [4]. The effect of the restricted wing span is to strengthen the wing tip vortices at high angles of attack, which in turn controls the flow. The measurements at University of Notre Dame [7-9] on rectangular flat plates of different aspect ratio at low Reynolds numbers showed that the lift curve was highly nonlinear for wings of aspect ratio below 1.25 and tend to become linear as the aspect ratio increases. The nonlinear lift in low aspect ratio wings at higher Reynolds number has been well documented by Polhamus [10]. He suggested that for thin wings, at low aspect ratios, the vortices have strong interactions with the flow on upper surface of the wing resulting in increased streamwise velocity on the upper surface, thus improving the

lift and delaying the stall. Recent works on MAV models [5,7,8] also attribute the same reason for the increase lift on MAV wing models.

Torres and Mueller [8,9] conducted a series of experiments on different planforms with varying aspect ratios at chord Reynolds number of 10,000. The results show that at an aspect ratio of 1.5, the elliptical and Zimmerman profiles provide higher maximum values of C_L and higher respective angle. They also perform better at lower aspect ratios (<1.5) and at high angles of attack. The inverse Zimmerman planform has higher control surface effectiveness and has its aerodynamic centre more aft as compared to regular configurations. These are highly favorable in terms of stability and control, particularly if the MAV is tailless.

Mukund and Karthikeyan [6] conducted force measurements in a wind tunnel on a variety of thin disc-shaped wings (planforms) with fuselage underneath to assess the effect of the planform shape and camber on the MAV performance. The result shows that lift continued to increase up to the maximum incidence tested of 38°; this kind of increase being aided by the leading edge separation bubble on the leeward surface of the wing; effective reattachment prevented stall. The inverse planform showed stall for the higher freestream velocities (V) of 12 and 15m/s at a lower angle, the minimum being at 28°. In these cases, on decreasing the incidence angle after stall, hysteresis was observed in lift. For lower V of 8 and 10m/s the lift curve did not indicate stall up to 38°. The lift coefficient and the maximum value of the L/D ratio were higher for cambered planforms compared to flat ones by at least 20%. The aerodynamic characteristics of the modified Zimmermann planform (MZ) combined with the camberline distribution of the Selig 4083 airfoil [11] designated as C1 camber had superior C_L and L/D ratio in the cruise range of incidence. Further, the planform area of MZ being higher than Zimmermann planform by about 4%, the lift forces would also be higher by the same amount.

3. MAV models

The MAV model used for the wind tunnel measurements consisted of a disc shaped wing fixed over a fuselage. The wing was made of a rigid composite sheet of about 2mm thickness. The wing planforms were either flat (designated C0) or had the camber distribution of the Selig S4083 airfoil (C1), schematic drawings of which are shown in Fig.1. Fig.2 shows the shape of planforms taken up in this study, of which, planform Z (Fig.2a) was based on the semi-ellipse pair suggested by Zimmermann [4]. Planform LZ (Fig.2b) was obtained by increasing the span of Z from 300 to 400mm. Planform MZ (Fig.2c) was modified from Z by adding a straight edge between the two semi-ellipses, increasing the wing planform area (by $\cong$ 4%). The rounded leading edge model (RLE) was obtained from the sharp leading edge the C1MZ planform by giving it a finite radius through the addition of composite material in the leading edge region as shown in the section drawings in Fig.2c and smoothened at the junctions. The maximum thickness of the added material was about 4.2% of the chord.

The nomenclature of the planform shapes and camber are listed in Table 1 & 2 respectively. The legends in the plots have the following generic designation Vvv-CcPPI, the symbol ‘vv’ stands for the freestream velocity in m/s, ‘Cc’ stands for the camber as given in see Table 1, PP stands for the planform (Table 2) and the final ‘I’, if present represents the inverse planform.

Camber	No camber	Selig 4083
Name	C0	C1

Table 1 Nomenclature of camberline used

Planform	Name	Span, mm	chord, mm	Area, mm^2	Aspect Ratio
Zimmermann	Z	300	280	65,900	1.37
Zimmermann with larger span	LZ	400	280	88,000	1.82
Modified Zimmermann	MZ	300	280	68,700	1.31
C1MZ with rounded leading edge	RLE	300	280	68,700	1.31
Inverse planform	I				

Table 2 Nomenclature and details of planforms used

All these planforms were fitted with a fuselage having standard frontal shape tapering towards the trailing edge as shown in Fig.3. The top surface of the fuselage was fixed to the bottom side of the wing using small screws and nuts. Different fuselages had to be fabricated depending upon the camberline distribution of each planform. The fuselage also housed the sting mounted force balance.

In the case of the powered propeller measurements, a brushless DC motor (AXI2203/54) was fitted to the leading surface of the fuselage and a two bladed MAV propeller (GWS7030) was fitted to its shaft. The motor rpm was electronically controlled using Phoenix 10 ESC and a custom made power supply.

4. Instrumentation

The wind tunnel freestream velocity was measured using a digital manometer of range ±20mm of H_20 from Furness Corp, UK. The force measurements on the MAV models were carried out using a 10mm-diameter six-component integral strain gauge balance of 2kg axial force designed and fabricated for the purpose. Pressure measurements were carried out on the upper surface along the central chordline of a pressure model of C1MZ. The model was fabricated with 31 flush-mounted pressure ports made of 1mm diameter stainless steel tubes. These tubes were connected through polyurethane tubes to a 32 port ±254mm H_20 range electronic pressure scanner from Pressure Systems, USA. The voltage output from the balance and the digital manometers were acquired and processed by means of a data acquisition card and LabVIEW® program from National Instruments, USA.

5. Measurements and uncertainty

Measurements were made at four freestream velocities as shown in Table 3

Freestream velocity V, m/s	Reynolds number
10	1.9×10^5
12	2.3×10^5
15	2.9×10^5
18	3.4×10^5

Table 3 Freestream velocity in the experiments and corresponding Reynolds numbers

The measurements were made on the MAV planform at low Reynolds number amidst unsteadiness caused by the separation bubble. In spite of which repeatability tests showed remarkable matching in the aerodynamic coefficients. Thus, the uncertainties estimated as a fraction of the full scale values were as follows.

$\Delta C_p \leq \pm 0.02 \times C_p$

$\Delta C_L \leq \pm 0.02 \times C_L$

$\Delta C_D \leq \pm 0.02 \times C_D$

Distance measurements done surface oil flow pictures have an uncertainty of 5%.

6. Results

a. Measurements on C1MZ planform

Force and static pressure measurements and surface oil flow visualization were conducted on the C1MZ planform at freestream velocities V in the range of 10 to 18m/s and incidence angle α in the range of -10 to 38°.

Fig. 4 shows the plots of the variations of the **aerodynamic coefficients** C_L, C_D, C_M and C_L/C_D with α at different V. The C_L plot shows that lift continues to increase up to α = 38° and stall has not occurred even at that high angle. No noticeable effect of freestream velocity is observed except that the higher freestream velocity (18m/s) data shows higher C_L/C_D at its maximum, occurring at $\alpha \cong 4°$. The lift curve can be split into several linear portions i.e., from -2 to 6°, 6 to 18°, 18 to 26° and 28 to 36° as indicated by the vertical dashed lines in the plots. Such multi-linear regions have been found in our data on other planforms as well as in [7,8] though they interpreted these as nonlinear regions.

The drag coefficient C_D (Fig.4) is small for $-5<\alpha<5°$ and increases beyond. The pitching moment curve shows linearity from -2 to 14° and again beyond 26° and is nonlinear in between.

The variation of the **surface static pressure distribution** over the central chordline is shown plotted in Fig.5a for V = 10, 12 and 15m/s and $0\leq \alpha \leq 25°$ and in Fig.5b for V =15m/s and $25\leq \alpha \leq 38°$. The profiles for the three freestream velocities are coinciding (Fig.5a), showing that the effect of α is more prominent than V. It also indicates the consistency of our measurements.

Fig.5a shows that the flow is attached at 0°, for $\alpha \geq 5°$, the flow is separated at the leading edge giving rise to large negative C_p; the sudden adverse pressure gradient downstream indicates reattachment to form a laminar separation bubble. The large region of negative pressures inside the bubble forms a basis for increased lift. The fact that C_p is not constant downstream and that lift continues to steadily increase (Fig.4) shows that the flow remains attached up to the trailing edge even at the highest angle. As α is increased up to 25°, the bubble reattaches at larger chordwise distances from the leading edge. Beyond 25° (Fig.5b), the length of the bubble remains constant, while the maximum suction pressure increases. Now, let us compare the results of the pressure measurements along the central chord line with the partwise linear regions of the lift curve. In the first linear region $0 < \alpha < 6°$, the suction peak occurs at the leading edge and the maximum negative pressure is increasing with angle. In the range $6° < \alpha < 18°$, the leading edge pressure becomes a constant and the negative pressure peak shifts aft. In the range $18 < \alpha < 26°$, the leading edge negative pressure decreases mildly, not changing with α and the location of the peak pressure moves further aft. In the incidence

range 28 < α < 36°, the leading edge negative pressure increases with angle, and the negative pressure near and at the trailing edge decreases.

The distance from the leading edge to the location of reattachment $x_{RA\text{-}PR}$ defined as the point where the sharp adverse pressure gradient starting the reattachment process meets the mild linear pressure gradient region downstream. The variation of the this distance with α is plotted in Fig.6 and shows that the distance to reattachment increases with α up to 25° after which it is constant as noted earlier.

Surface **oil flow visualization** studies were conducted on the C1MZ model at V=15m/s. Let us first study the picture for α=15° in Fig.7 before analyzing other angles. The red dash in the figure refers to the reattachment distance $x_{RA\text{-}PR}$ from derived from pressure data (Fig.6). The yellow colored line represents reattachment. As may be noticed, the reattachment along the central chordline is at a larger chordwise distance compared to the rest possibly affected by the large frontal surface area of the fuselage underneath. However, as we shall see in the next section (6b) this would not affect the aerodynamic characteristics of the planform.

It may also be noted that the reattachment line along the central line matches with the red dash ($x_{RA\text{-}PR}$). Here, we find two regions where the oil dots have not moved. Firstly the leading edge region and secondly the region near the centre encompassed by the dashed and the solid lines. These are reverse flow regions in the front and aft parts of the bubble respectively, where, the shear is insufficient to move the oil dots. Downstream of the reattachment line, the flow is generally in the streamwise direction. The tip vortices also have regions of no-flow close to the tip and the flow inside the vortex is at an angle to the freestream direction. Towards the trailing edge downstream, it merges smoothly with main streamwise flow.

The oil flow pictures at other angles for the C1MZ model are presented on the left side of Fig.7b. The pictures on the right side are from the rounded leading edge experiments discussed subsequently. These show similar events at other angles too, though not very distinct at lower angles. Reattachment moves downstream as α is increased, to positions along the central line roughly coinciding with the red dash. At α=20° and 25°, there is a strong interaction between the reattachment line and the tip vortex forming a complicated flow pattern. At α=25°, the reverse flow region occupies most of the planform area but the attached flow region occupies a distinct part in the last 10% chord. The width of the tip vortices increase with angle of attack and we observe an enhanced interaction with the separated flow.

It may be noticed in the pressure plots for α = 15, 20 and 25° (Fig.5) that the end of the favourable pressure region at 9, 18 and 30%c respectively closely corresponds to the location in the oil flow pictures (Fig.7) along the central line of the junction between the reverse flow streaks and the no-flow dots.

b. Effect of rounded leading edge

The oil flow visualization pictures for the planforms with rounded leading edge (RLE) are presented on the right side in Fig. 7b for different specified angles. These are compared with the pictures for sharp leading edge (already introduced). The figures show that leading edge separation occurs in both cases. There is no remarkable difference in the reattachment position at α=5 and 10° and seems to be earlier for RLE at α=15 and 20°. At α=25°, the reattachment zone is so long that the differences in the reattachment cannot be adjudged clearly. The aerodynamics characteristics comparing the two leading edge conditions presented in Fig.8

confirm what was observed in the oil flow pictures that there is not much of a difference between the two. This exercise shows that the thickening of the leading edge region to the extent of about 4% of the chord did not help avoiding the leading edge separation or in improving the aerodynamic characteristics. By increasing the leading edge radius further, it may be possible to achieve an optimized condition of having attached flow and lower drag at cruise α and leading edge separation bubble at higher α; effectively pushing stall to very high angles.

c. Effect of Larger span

Experiments were conducted comparing flat Zimmerman planform C0Z and its inverse C0ZI, considered to be of normal span, with planforms having larger span namely, C0LZ and C0LZI. Refer to Fig.2a,b and Table 1 and 2 for respective shapes, sizes, flow direction and nomenclature.

The aerodynamic coefficients at three freestream velocities comparing the normal planforms C0Z with C0LZ are plotted in Fig.9 and comparing the inverse planforms in Fig.10. Colored sketches of the planforms shown act as a legend for the C_L, C_D and C_M plots. The lines for the three velocities - plotted in identical colours to improve clarity - highlight that the freestream velocity variation has little effect on these three parameters.

The results for the larger span models show that they too have two linear regions, having comparatively higher lift slope. For $\alpha > 15°$ the lift of the larger span models show a large decrease in the slope indicating the starting of stall. However, the lift for the normal span continue to increase; C0Z planform had not stalled even at α=38°, whereas in the case of its inverse (C0ZI) its C_L reaches its maximum value at α=28°. In both cases, the inverse planforms stall earlier than the regular counterparts. Though zero lift is expected at α=0° on these flat planforms, we observe that C_L becomes positive at a small positive angle, which can be ascribed to the presence of the fuselage underneath.

The lift induced drag follows the lift curve as expected. C_{Do} (= C_D under zero lift condition) is plotted in Fig.11 comparing the four configurations and three velocities. The figure shows firstly, that C0Z has lower C_{Do} than the other three planforms at all velocities. Secondly, there is a general improvement in C_{Do} with increase in V. However, it may be noted that these values though consistent are too small to be noted in the big picture in Fig.9 and 10.

The slope of the pitching moment curve in Fig.9,10 is positive for regular planforms and negative for the inverse planforms. This is expected as the inverse planforms are aft loaded. The L/D ratio is plotted in different colors to differentiate the small differences. L/D values attain their maximum value between $5° < \alpha < 7°$, generally the value improves with freestream velocity and for larger span.

The oil flow pictures comparing the four planforms are presented from Fig.12-17 for six specified incidence angles. The figures show well defined reverse flow and reattachment regions in all the cases. The central chord region has reattachment at a farther distance being affected by the presence of the fuselage underneath. On comparing, we see that the larger span planforms have reattachment at a larger distance. The normalized chordwise distances from the leading edge at which reattachment occurs along the central line (x_{RA}/c) are plotted in Fig.18a and the values at a spanwise distance half way to the tip (x_{RA50}/c) in Fig.18b. The values of x_{RA50}/c could not be adjudged clearly for α=20° and are not plotted in Fig.18. The oil flow picture and the plots show that reattachment takes place at increased distances with α, reattachment is

postponed for larger span planforms at all angles and the inverse planforms have earlier reattachment comparatively. At α=20°, the flow is fully separated for the larger span planforms while reattachment is observed for the normal span planforms. The oil flow picture for C0ZI at α=20° (Fig.16) clearly shows the dramatic interaction between the tip vortices and the separated flow to enable reattachment.

d. Effect of powered propeller

Force measurements and surface oil-flow visualization were conducted on the C1MZ model with powered propeller. Initially force measurements were conducted at three freestream velocities and four angles at different propeller rotation rates (rpm). This exercise helped determine the minimum rpm at which thrust becomes positive (negative drag) for each flow condition. The aerodynamic coefficients from selected runs are plotted in Fig.19, 20. The comparison plots at α=0 and 10° (Fig.19) shows, as expected, that C_L is nearly constant for α=0° at all rpm and freestream velocities V, showing an increasing trend for α=10° on increasing V. C_D naturally decreases with increased rpm or V, implying that it requires higher rpm at higher velocities to produce the same thrust coefficient. Comparisons at the same freestream velocities (Fig.20) show that at higher angles of attack it requires a higher rpm to produce larger thrust to compensate for the increased drag.

Force measurements were conducted at selected rpm and V for α in the range of -2 to 25°, the aerodynamic coefficients of which are plotted from Fig.21-22. Fig.21 gives a comparison at different freestream velocities at a fixed rpm of 7200. On comparing the results with / without the propeller for V =15m/s, we see that C_L values match up to $\alpha \cong$15°, beyond which it increases slightly for the propeller case and that C_D is consistently lower for the propeller case at all angles. With increased V, the slope of C_L increases and C_D decreases. As rpm is increased (Fig.22) from 7200 to 8400 holding V constant at 15m/s, the C_L slope increases initially but does not respond on further increase to 9000rpm, while C_D decreases continuously.

In order to segregate the influence of drag on lift coefficient, the aerodynamic coefficients were resolved in the normal and axial directions (to obtain C_N and C_A respectively) and are shown plotted in Fig.23. Here, we see that the C_N and C_L match with each other up to about $\alpha \cong$ 18° after which C_L reduces marginally as can be expected. Both C_A and C_D start negative and beyond $\alpha \cong$ 5° the lift induced drag influences C_D to become positive and increase, while C_A continues to decrease with increasing angle due to the decreased dependency on the normalizing component V with angle.

Surface oil flow pictures on C1MZ planform with propeller at 9000 rpm are compared with oil flow pictures without propeller in Fig.24 for V =15m/s and α = 20° and 25°. While the pictures without the propeller show reattachment at about 65% and 80% chord for the two angles respectively, with propellers reattachment occur much earlier at about 25% chord. Further, with propeller, the flow is asymmetric about the central span with a distinct spanwise flow from left to right side, this matches with the direction of rotation of the propeller.

In general, one of the effects of the propeller is to advance the reattachment of the flow separated at the leading edge. The reattachment however, does not deteriorate the aerodynamic characteristics of the planform and in fact, along with an expected decrease in drag, lift increases for high rpm of the propeller. Thus, we can say that the force measurements conducted without the propeller act as a conservative estimate of the lift characteristics of

planform for evaluating the performance with powered propeller, over which corrections may be applied for improving the estimates.

7. Conclusions

Wind tunnel measurements were conducted on MAV planforms to understand the flow over such planforms and study conditions necessary for improving the flow to achieve better aerodynamic characteristics.

Force measurements conducted on these planforms show that lift continued to increase up to α = 38°, without stalling even at that high angle, whereas inverse planforms stalled at about 28°.

The surface static-pressure distribution over the central chord-line showed that the flow separated at the leading edge for $\alpha \geq 5°$ giving rise to large negative C_p, the sudden adverse pressure gradient downstream showed reattachment of the laminar separation bubble. The location of reattachment moved aft as the angle was increased up to 25° at and beyond which the reattachment location occurred at a constant distance of about 80%c.

The oil flow pictures over the MAV planforms vividly illustrate the presence of the leading edge separation, its reattachment and attached flow thereafter. The width of the two tip vortices observed increased with angle and they interacted with the separated flow to promote reattachment.

The rounding of the leading edge with a diameter of 4% chord altered neither the aerodynamic coefficients nor the oil flow patterns grossly.

Planforms with larger span showed earlier stall and delayed reattachment. The oil flow patterns clearly showed that the tip vortices played a major role in the planforms with normal span and their role became weaker as the span was increased.

The role of the tip vortex in reattachment is clearly seen in the following -

- no stall up to large incidences
- earlier stall for inverse planforms due to aft loading
- reattachment point from pressure measurements at high angles are same
- oil flow pictures clearly showed interaction between the tip vortex and lsb
- models with larger span reattached later and stalled earlier compared to those with normal span due to increased interaction distance to central span

The force measurements conducted with powered propeller on the MAV planform showed that the powered propeller altered the slope of the lift line, had a negligible effect on the normal force coefficients for α<15°, beyond which there was a small increase. While the drag coefficient became negative with increased rpm, the axial force coefficient was always negative and became more negative with increased incidence. The oil flow pictures show earlier reattachment and asymmetric patterns.

Acknowledgements

The authors wish to thank the staff members of EAD model shop for fabricating the models, of the wind tunnel for their contributions to the experiments and of the MAV unit of NAL for supplying the motors and propellers. Special thanks to D.C. Enterprises, Bangalore for designing a propeller motor controller.

References

1. Carmichael B.H (1981) *Low Reynolds Number Airfoil Survey*, Vol. 1, NASA CR 165803.
2. Lissaman P.B.S (1983) *Low Reynolds Number Airfoils*, Annual Review of Fluid Mechanics, 15:223-239.
3. Mueller T.J and DeLaurier D (2003) *Aerodynamics of Small Vehicles*, Annual Review of Fluid Mechanics 35:89-111.
4. Stanford B, Ifju P, Albertani R, Shyy W (2008) *Fixed membrane wings for micro air vehicles: Experimental characterization, numerical modeling, and tailoring*, Progress in Aerospace Sciences, 44:258-294.
5. Zimmerman C.H, *Characteristics of Clark Y airfoils of small aspect ratios*, NACA TR 431,1932.
6. Mukund R. and Karthikeyan N, *Experimental investigations and evaluation of MAV planforms*, NAL PD EA 0921, National Aerospace Laboratories, Bangalore, India, 2009.
7. Pelletier A and Mueller T.J, *Low Reynolds Number Aerodynamics of Low Aspect Ratio Wings*, AIAA 99-3182.
8. Torres G. E, and Mueller T.J, *Low Aspect Ratio Wing Aerodynamics at Low Reynolds Number*, AIAA Journal, Vol. 42, No 5, 2004, pp. 865-873.
9. Torres G. E, and Mueller T.J, *Aerodynamics of Low Aspect Ratio Wings at Low Reynolds Number with Applications to Micro air vehicle Design and Optimization*, UNDAS-FR-2025, University of Notre Dame, 2001
10. Polhamus E.C., *A concept of vortex lift of sharp-edge delta wings based on leading edge suction analogy*. Technical Report TN D-3767, NASA, 1966.
11. Selig M.S, Guglielmo J.J, Broern A.P and Giuere P, *Summary of Low – Speed Airfoil Data*, V1, SoarTech Publ., 1995.
12. Selig M.S, Lyon C.A, Guglielmo J.J and Giuere P, *Summary of Low – Speed Airfoil Data*, V2, SoarTech Publ., 1996.
13. Selig M.S, Lyon C.A, Guglielmo J.J, Giuere P and Gopalarathnam A, *Summary Of Low – Speed Airfoil Data*, V3, SoarTech Publ., 1998.

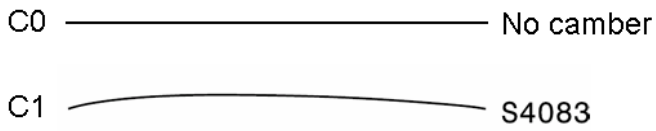

Fig.1 Mean camber line distributions

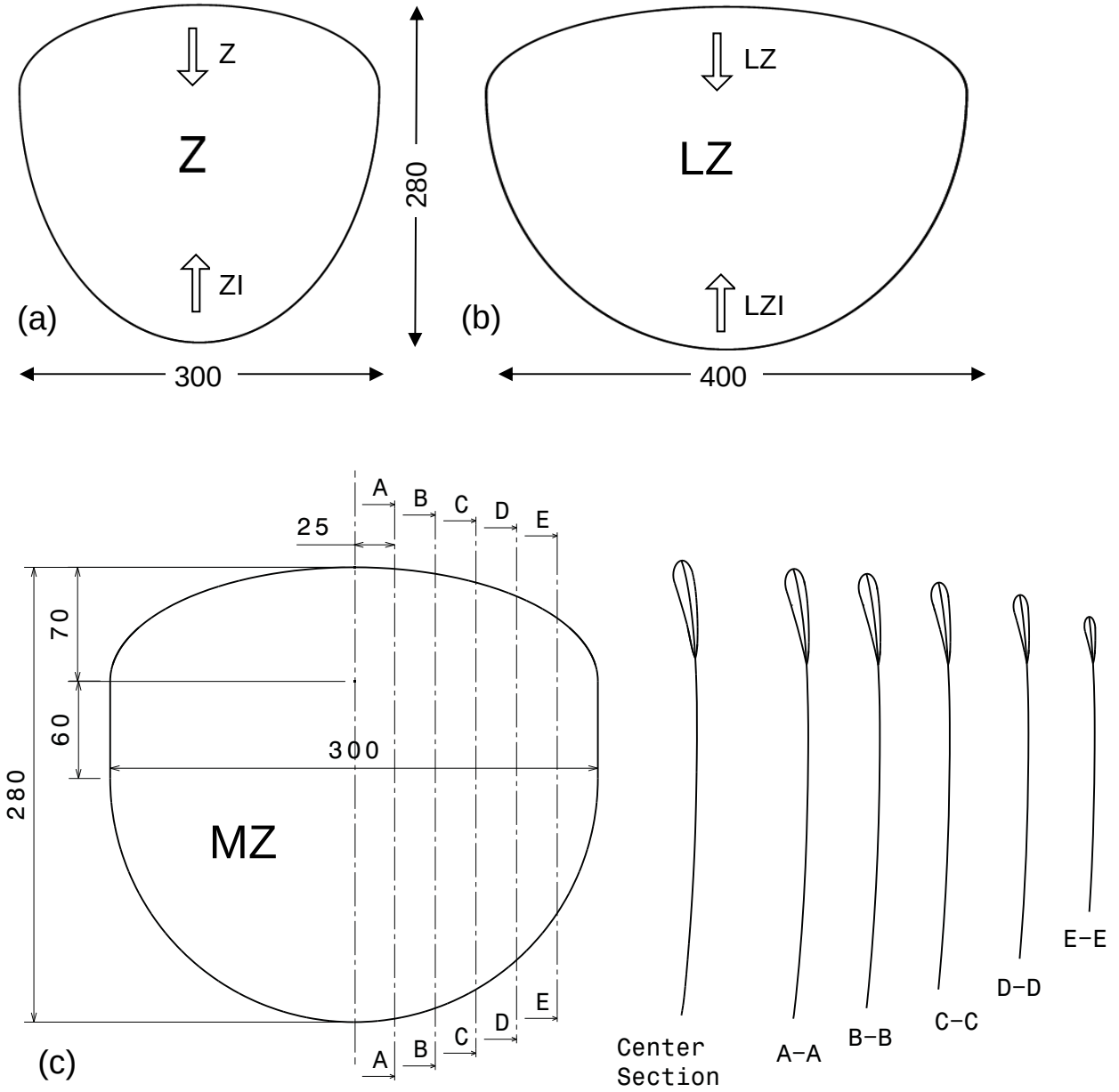

Fig.2 The planform shapes used for the experiments. All dimensions are in mm. Arrows in Fig.2a,b indicate flow direction for respective planforms and their inverse.

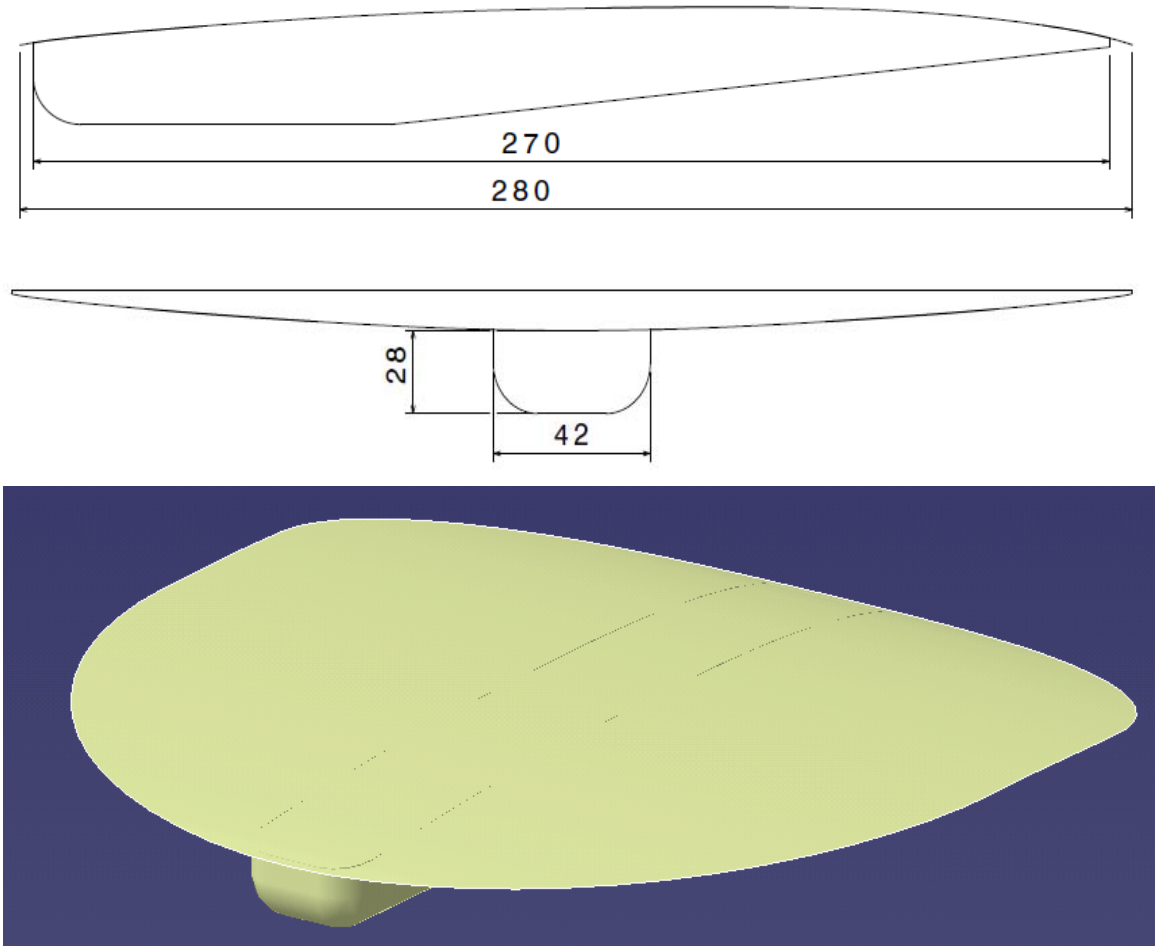

Fig. 3 Assembly of the planform with contoured fuselage

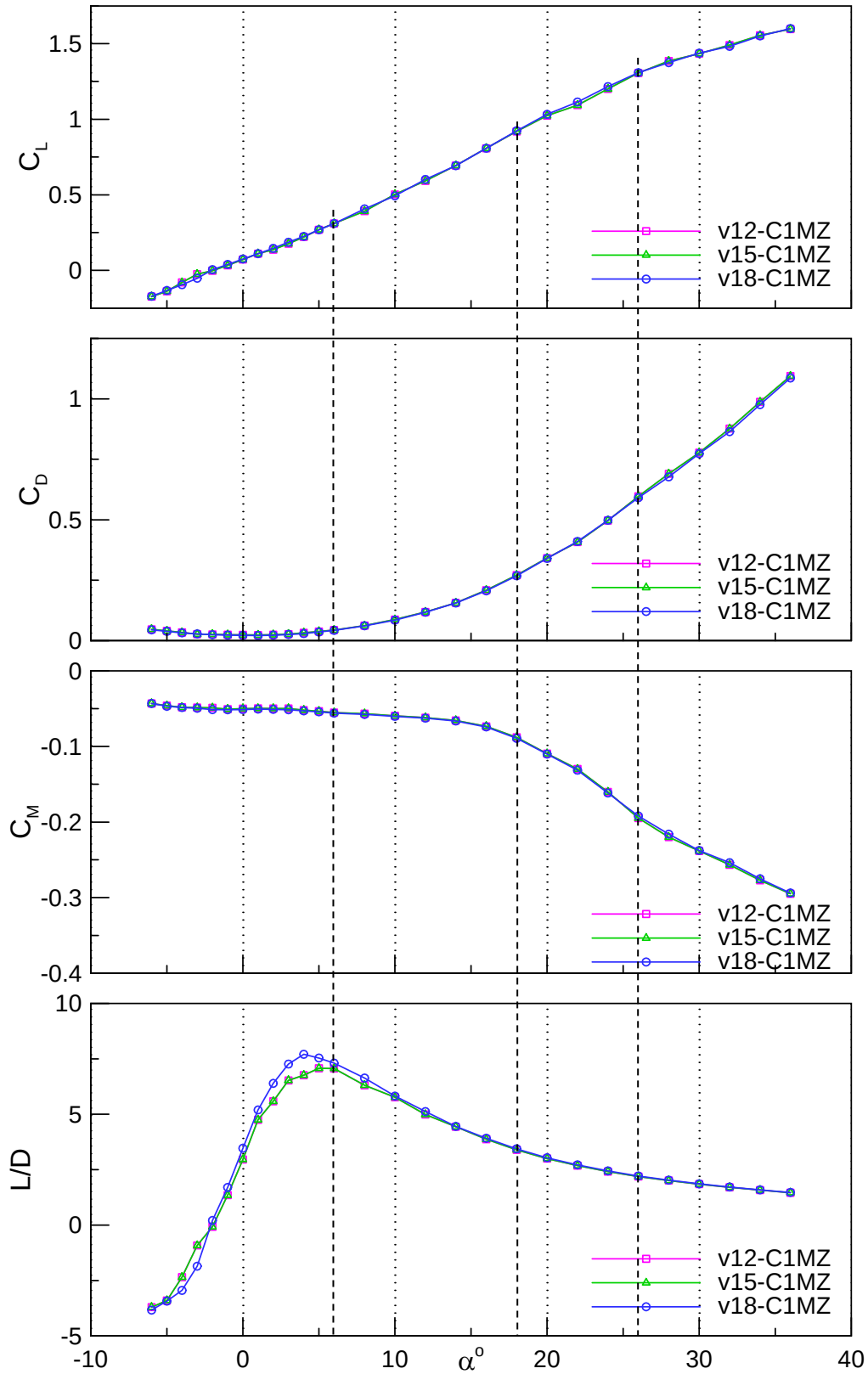

Fig. 4 Aerodynamic coefficients of C1MZ planform at three freestream velocities V = 12,15 and 18m/s as indicated in the legend

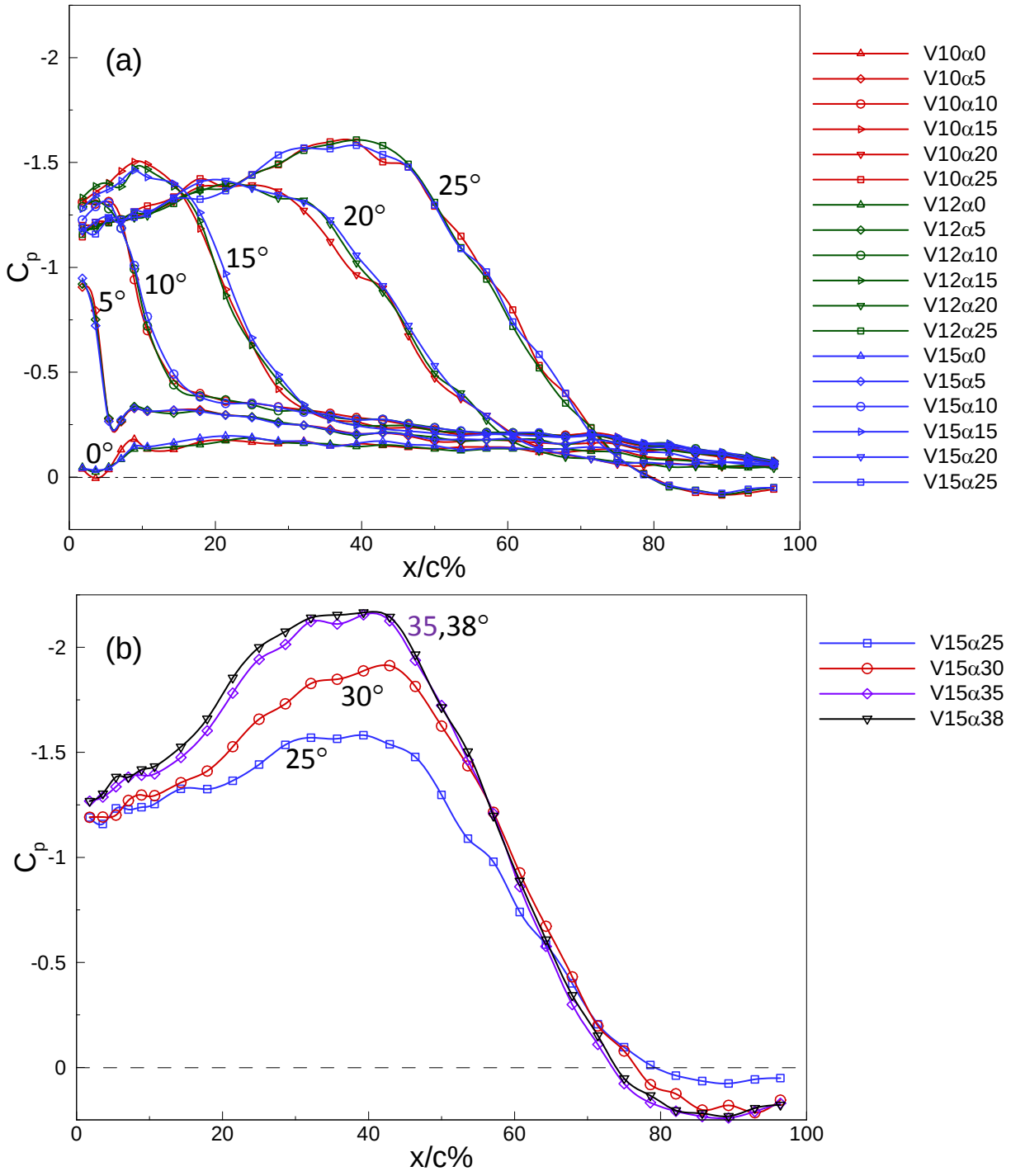

Fig.5 Pressure distribution on the centerline of the C1MZ planform at V=10,12 and 15m/s and α = 0 to 38° as indicated in the legend

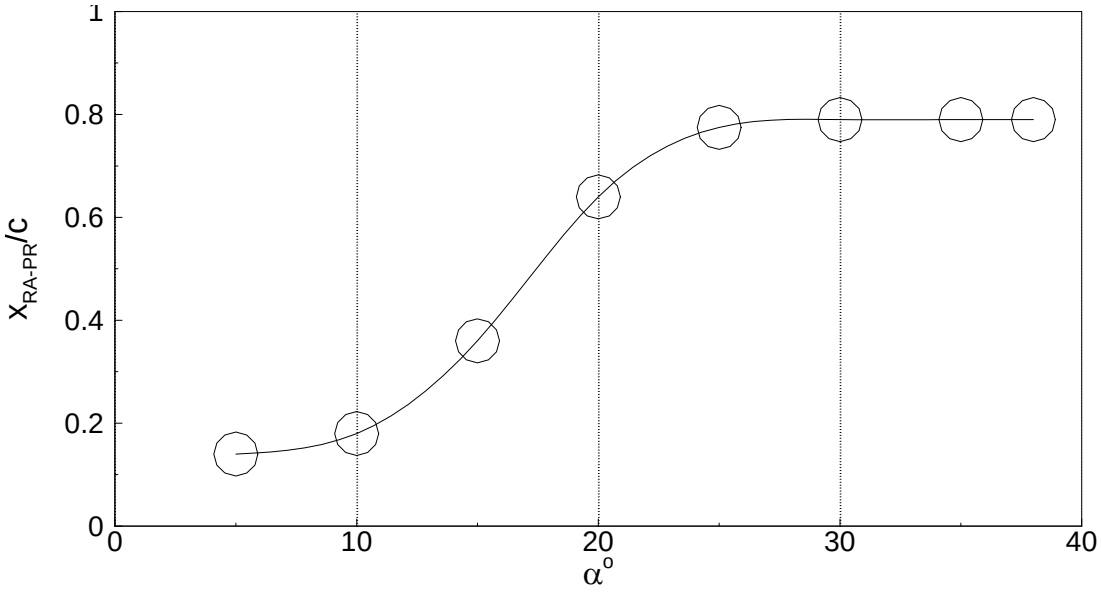

Fig.6 Reattachment point on the centerline of the C1MZ planform assessed from pressure data in Fig.5a. The point is junction between the sharp adverse pressure gradient and the downstream linear pressure distribution

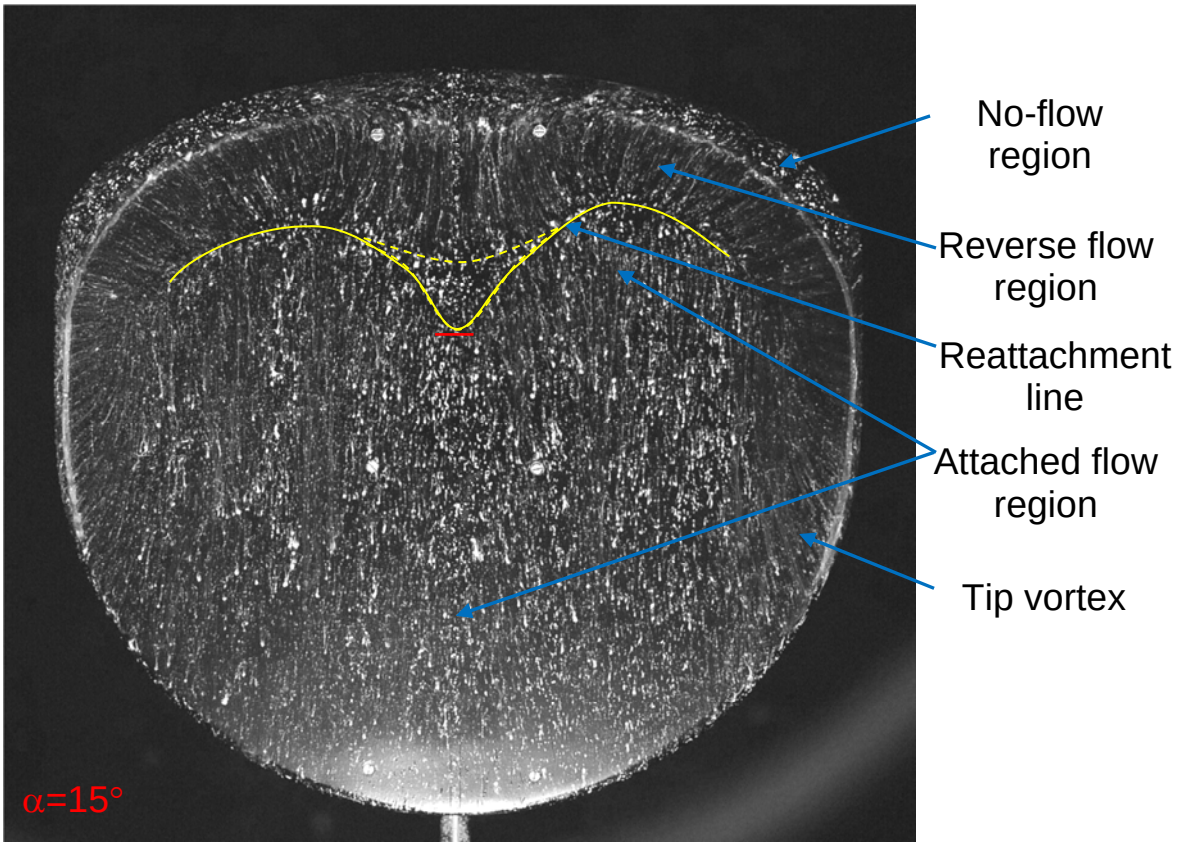

Fig. 7a Photographs of oil flow visualization on C1MZ planform at α=15° and V=15 m/s

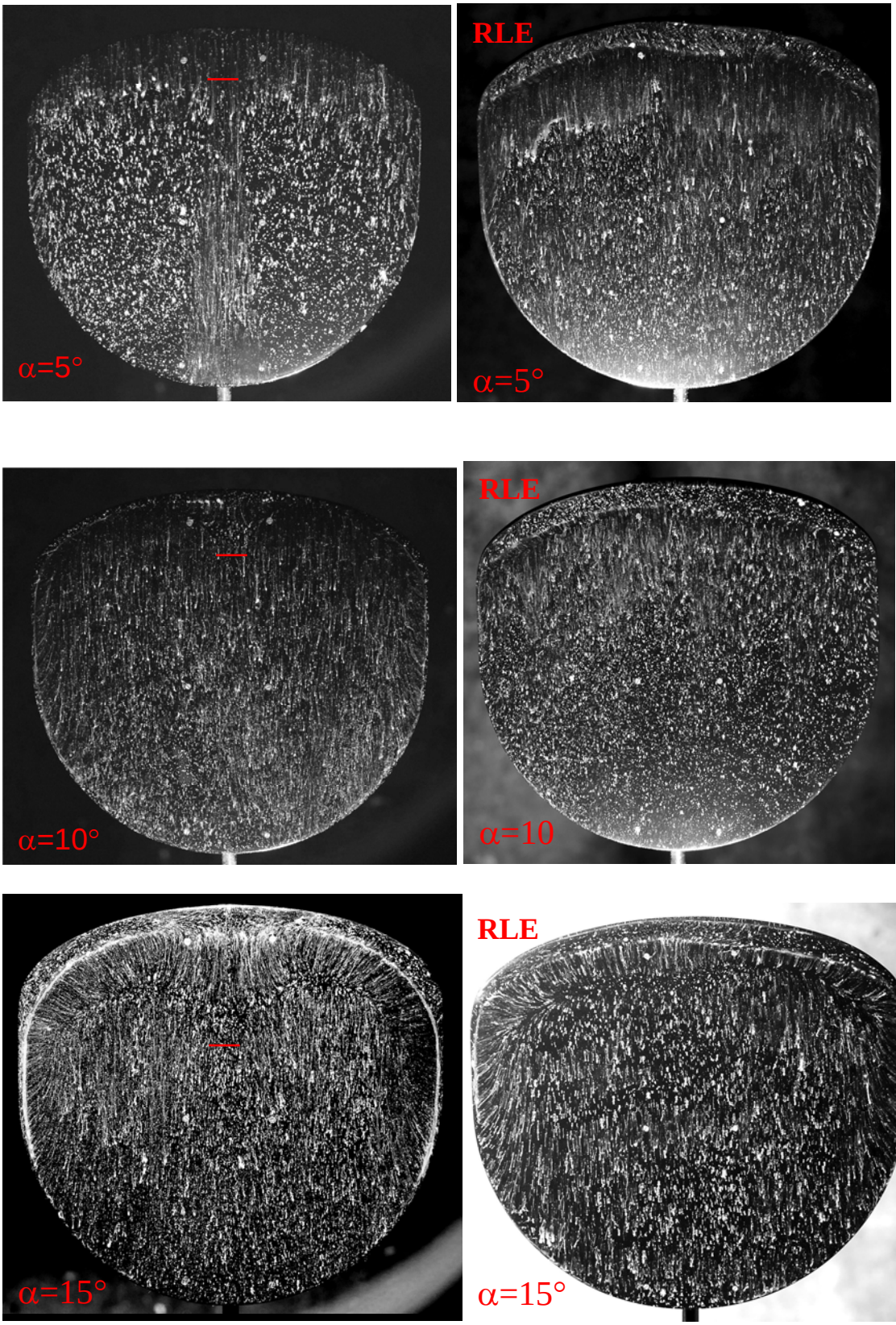

Fig.7b Photographs of oil flow visualization on C1MZ planforms with sharp leading edge (left side) and rounded leading edge (RLE) at V=15 m/s

-----continued

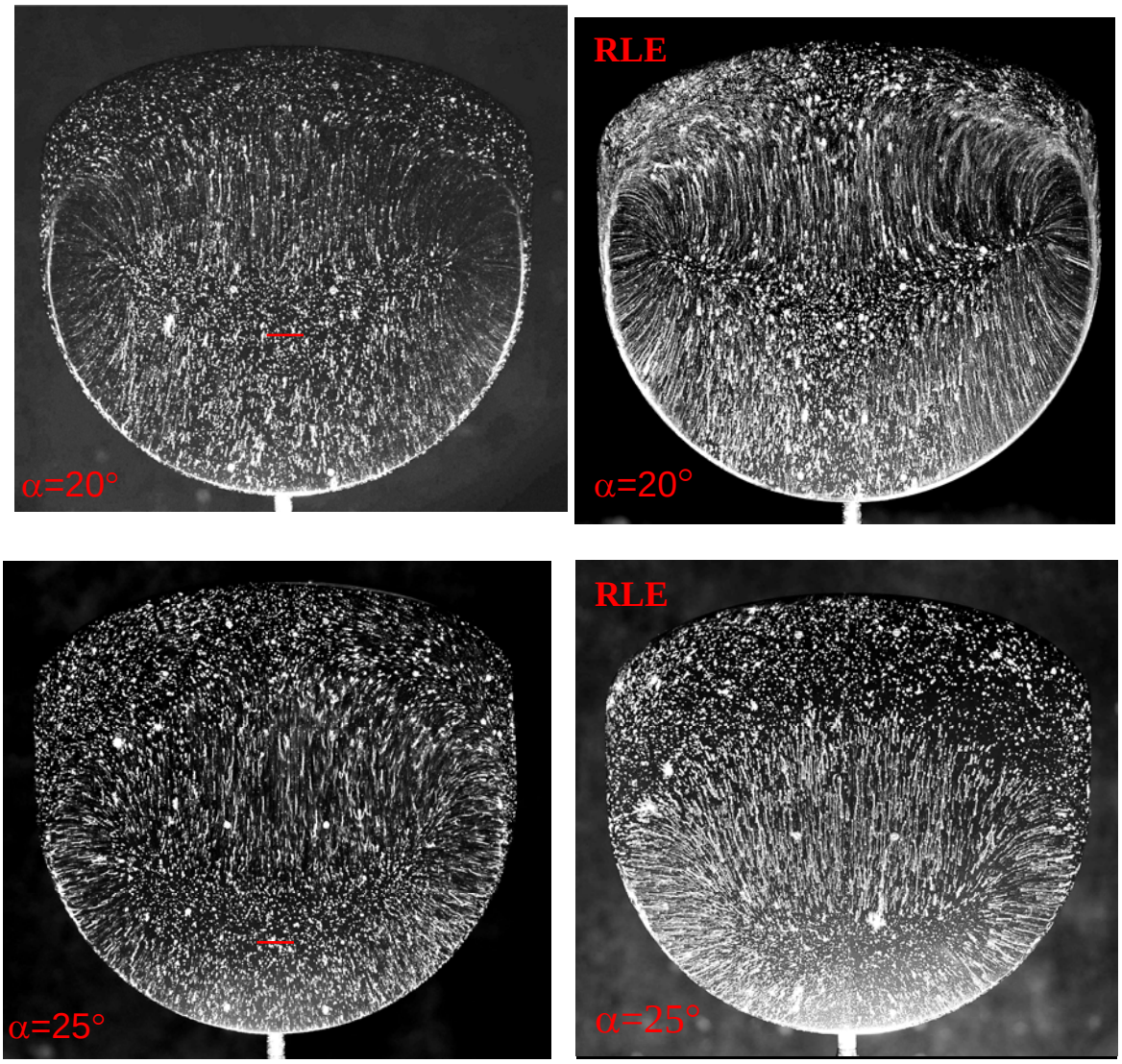

Fig.7b Photographs of oil flow visualization on C1MZ planforms with sharp (left side) and rounded (RLE) leading edges at V=15 m/s

-----concluded

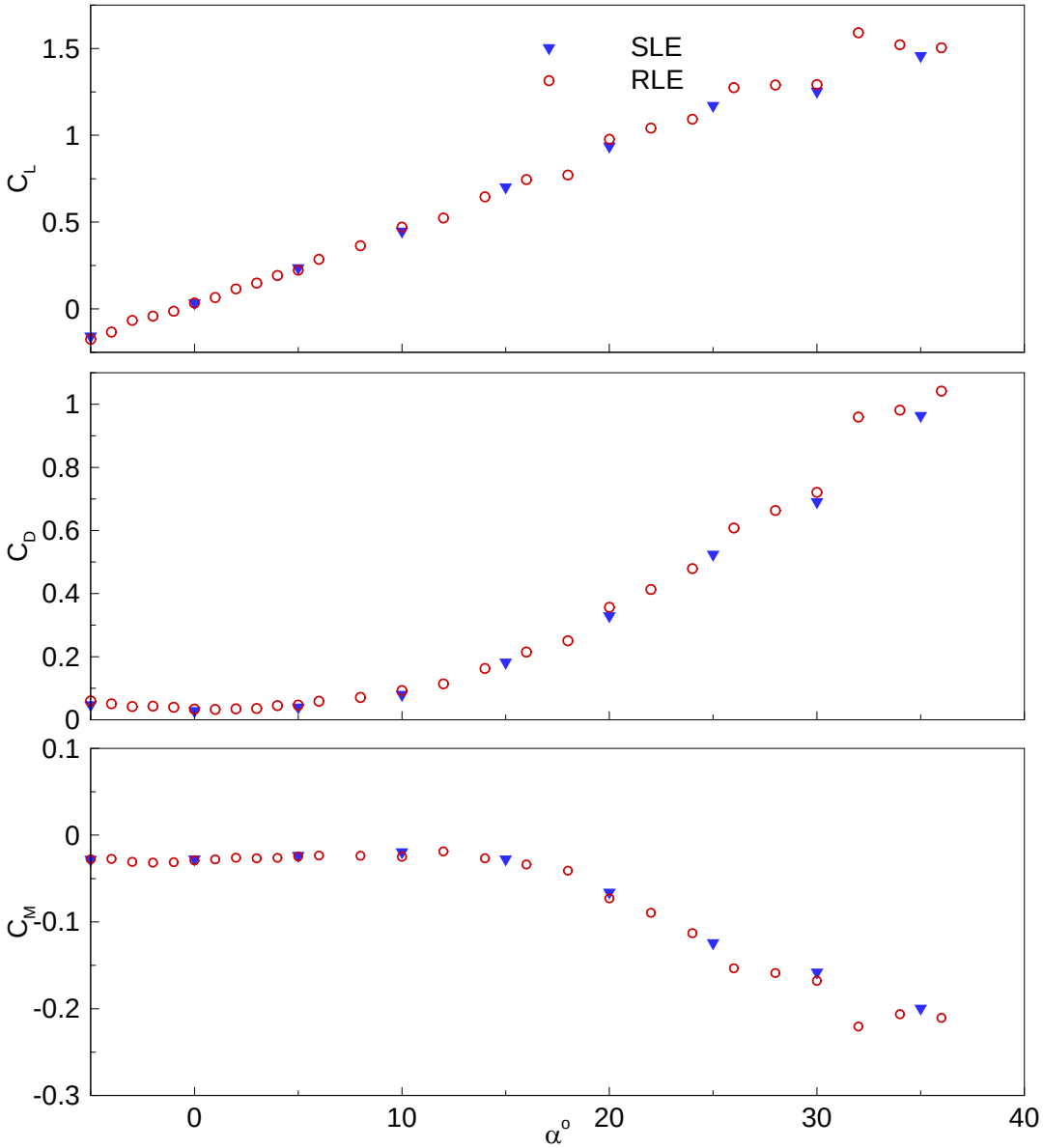

Fig.8 Aerodynamic coefficients of C1MZ planform with sharp (SLE) and rounded (RLE) leading edges at V=15 m/s

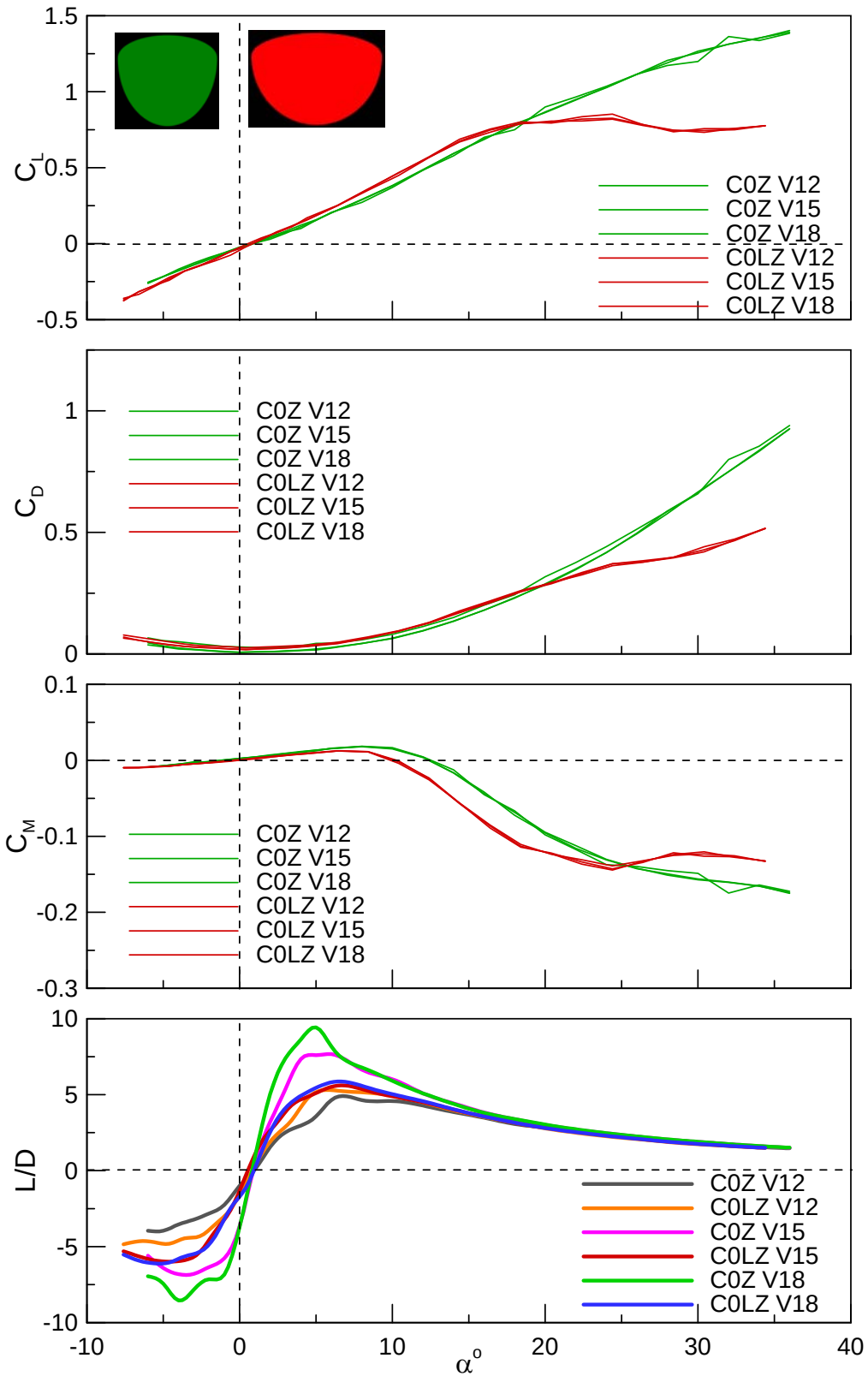

Fig.9 Aerodynamic coefficients comparing normal and larger spans C0Z and C0LZ

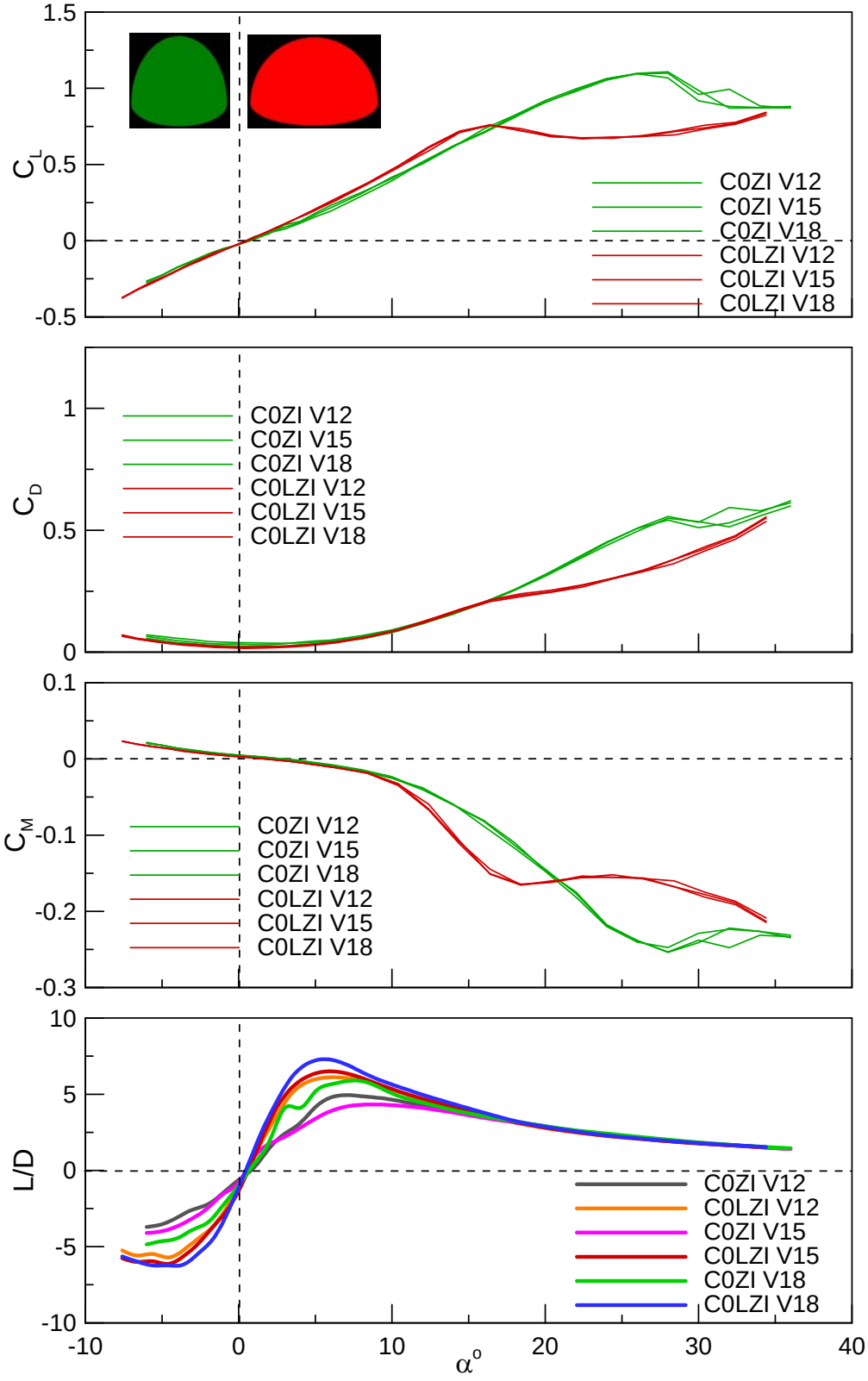

Fig.10 Aerodynamic coefficients comparing normal and larger spans C0ZI and C0LZI

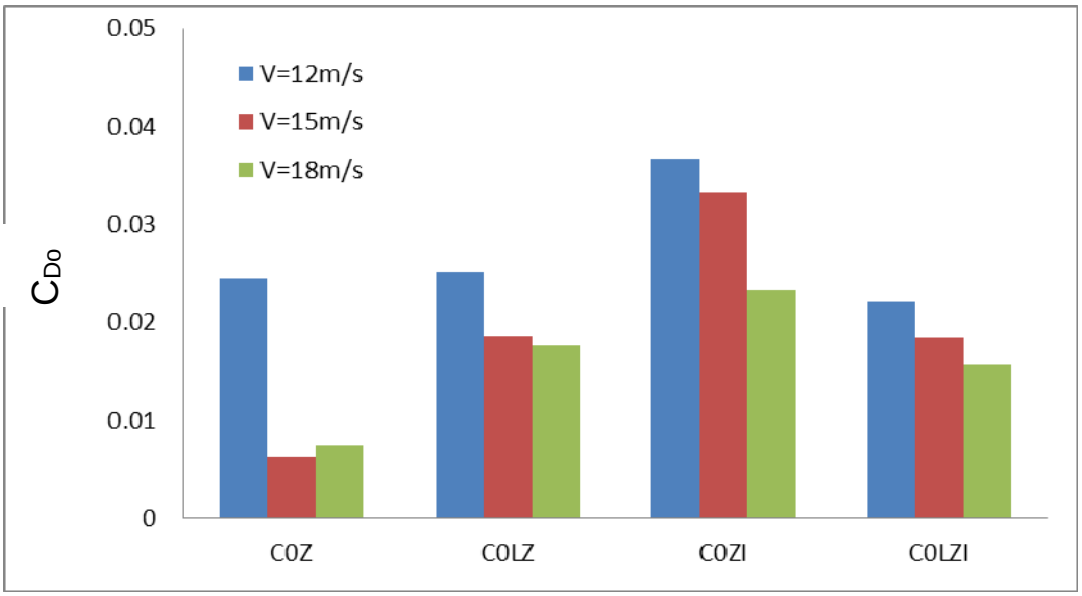

Fig.11 Comparison of C_{Do} for the four configurations at three freestream velocities

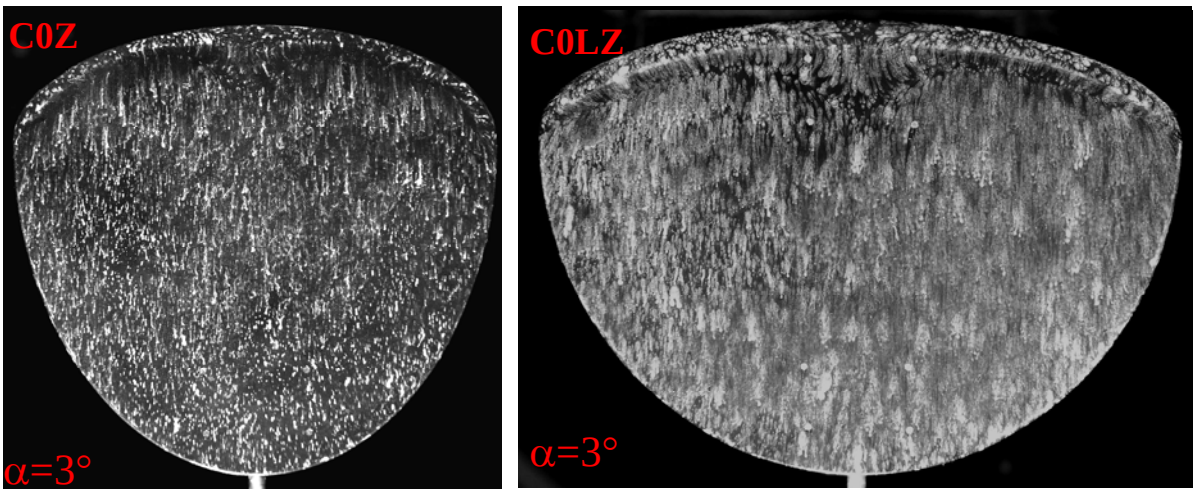

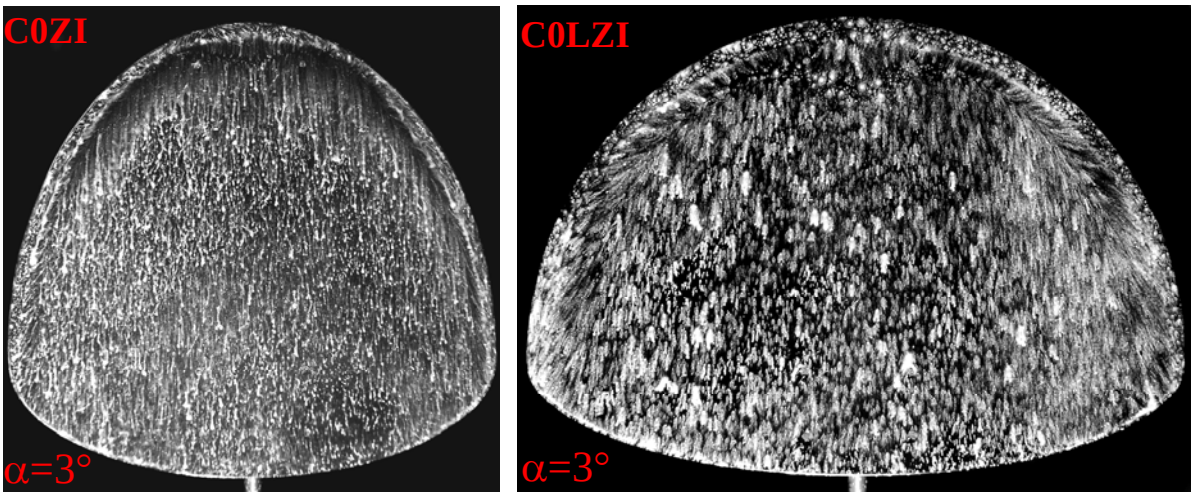

Fig.12 Oil flow visualization photographs comparing normal and larger planforms C0Z and C0LZ and their inverse C0ZI and C0LZI at α=3°.

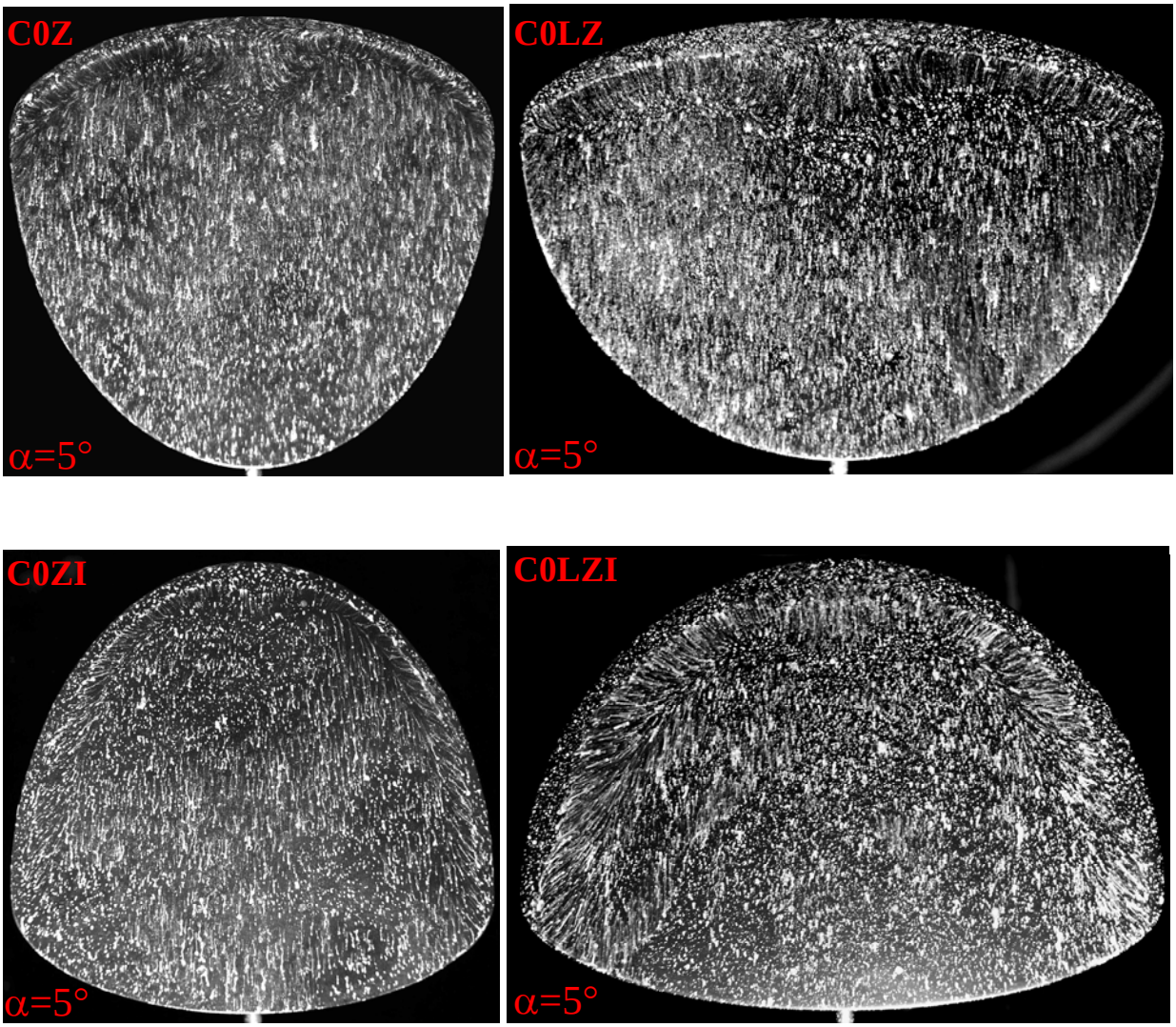

Fig.13 Oil flow visualization photographs comparing normal and larger planforms C0Z and C0LZ and their inverse C0ZI and C0LZI at α=5°.

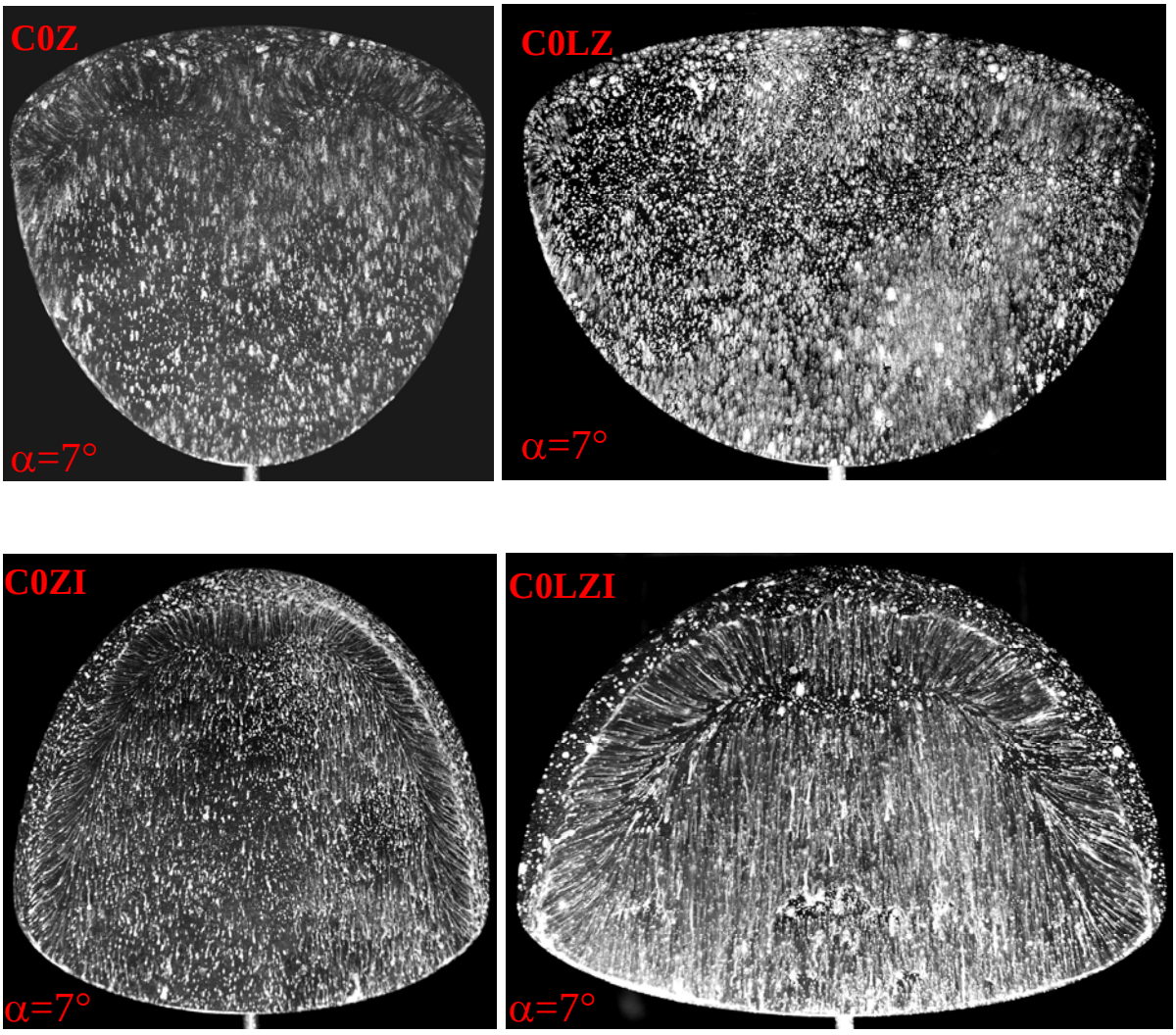

Fig.14 Oil flow visualization photographs comparing normal and larger planforms C0Z and C0LZ and their inverse C0ZI and C0LZI at α=7°.

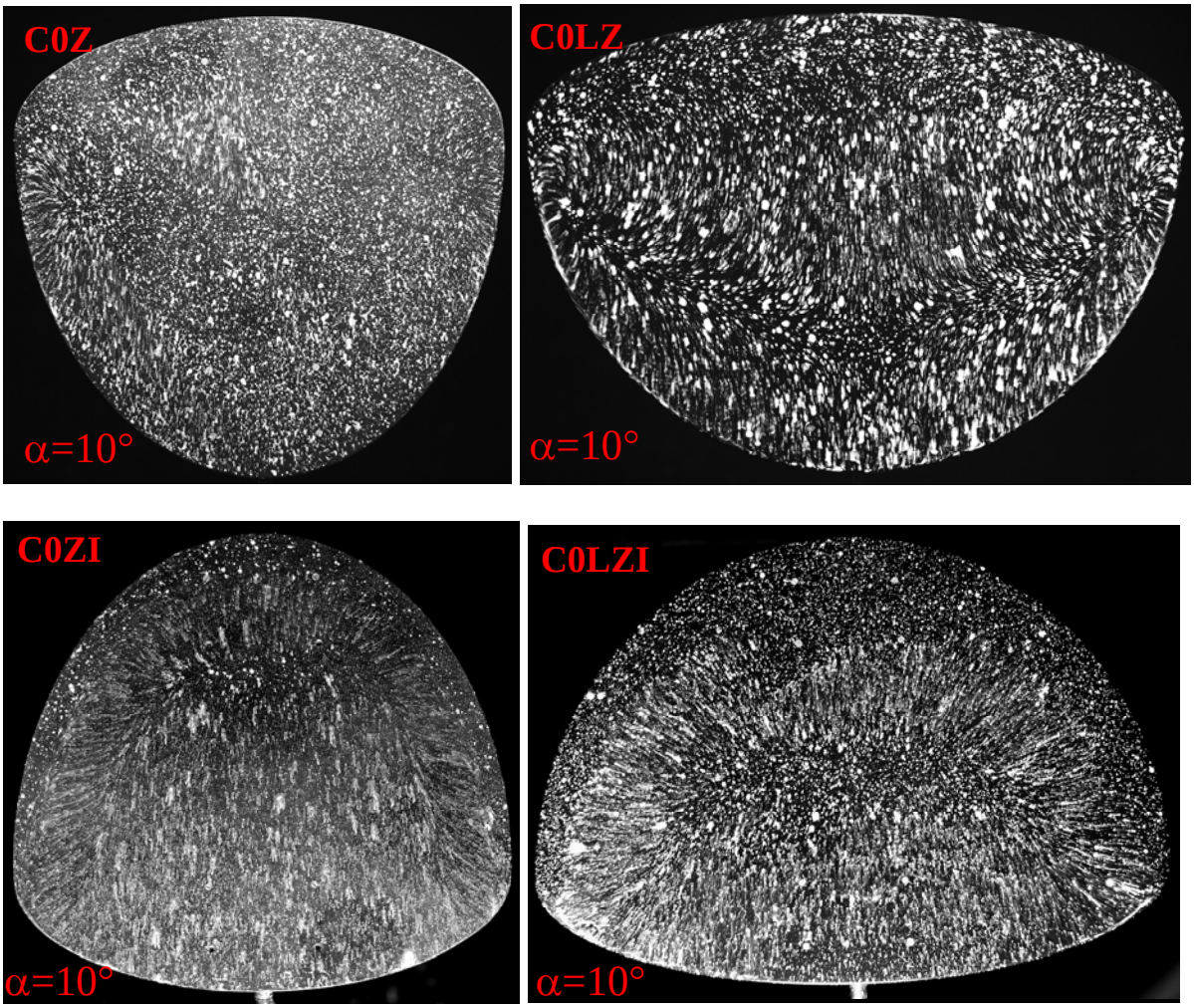

Fig.15 Oil flow visualization photographs comparing normal and larger planforms C0Z and C0LZ and their inverse C0ZI and C0LZI α=10°.

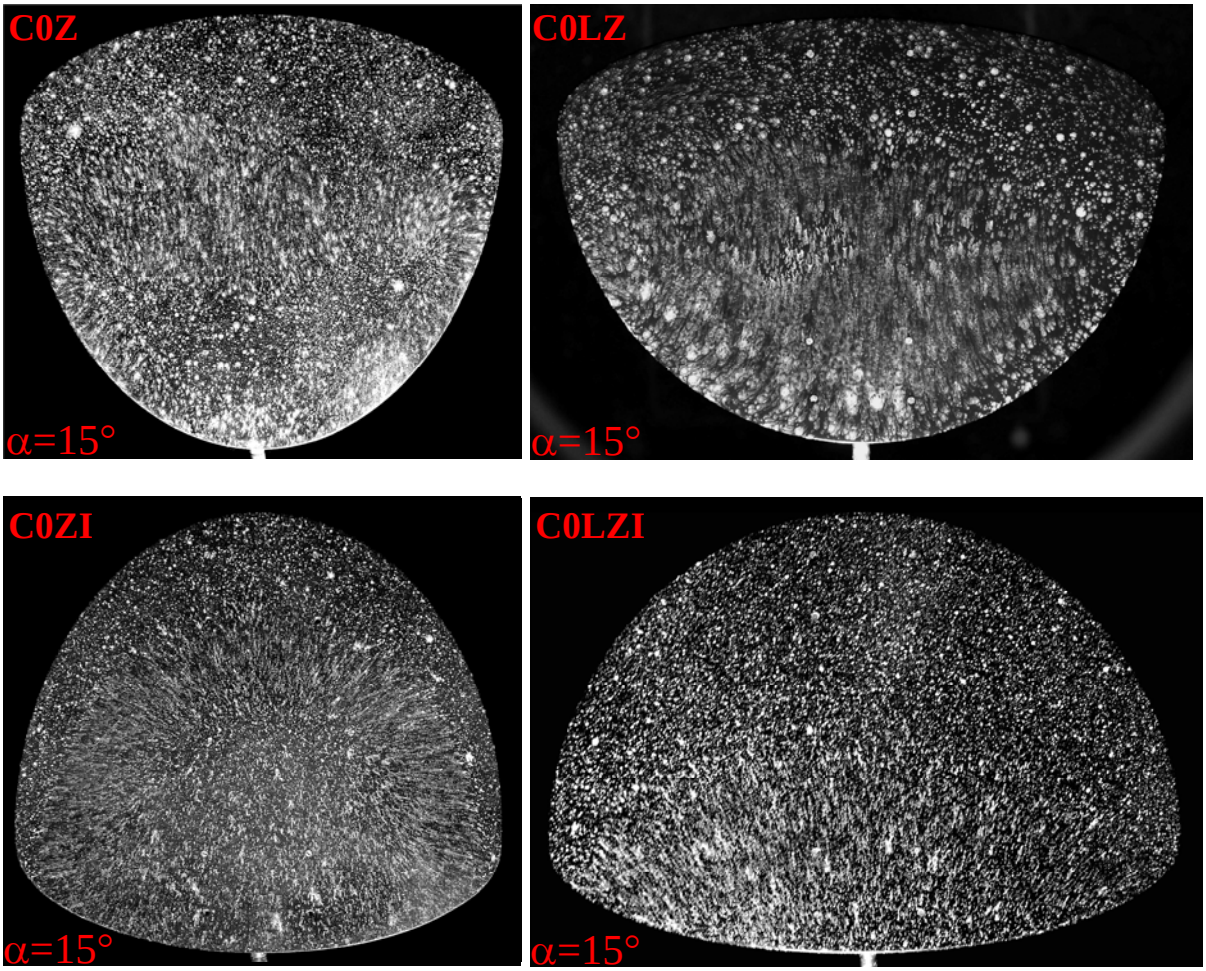

Fig.16 Oil flow visualization photographs comparing normal and larger planforms C0Z and C0LZ and their inverse C0ZI and C0LZI α=15°.

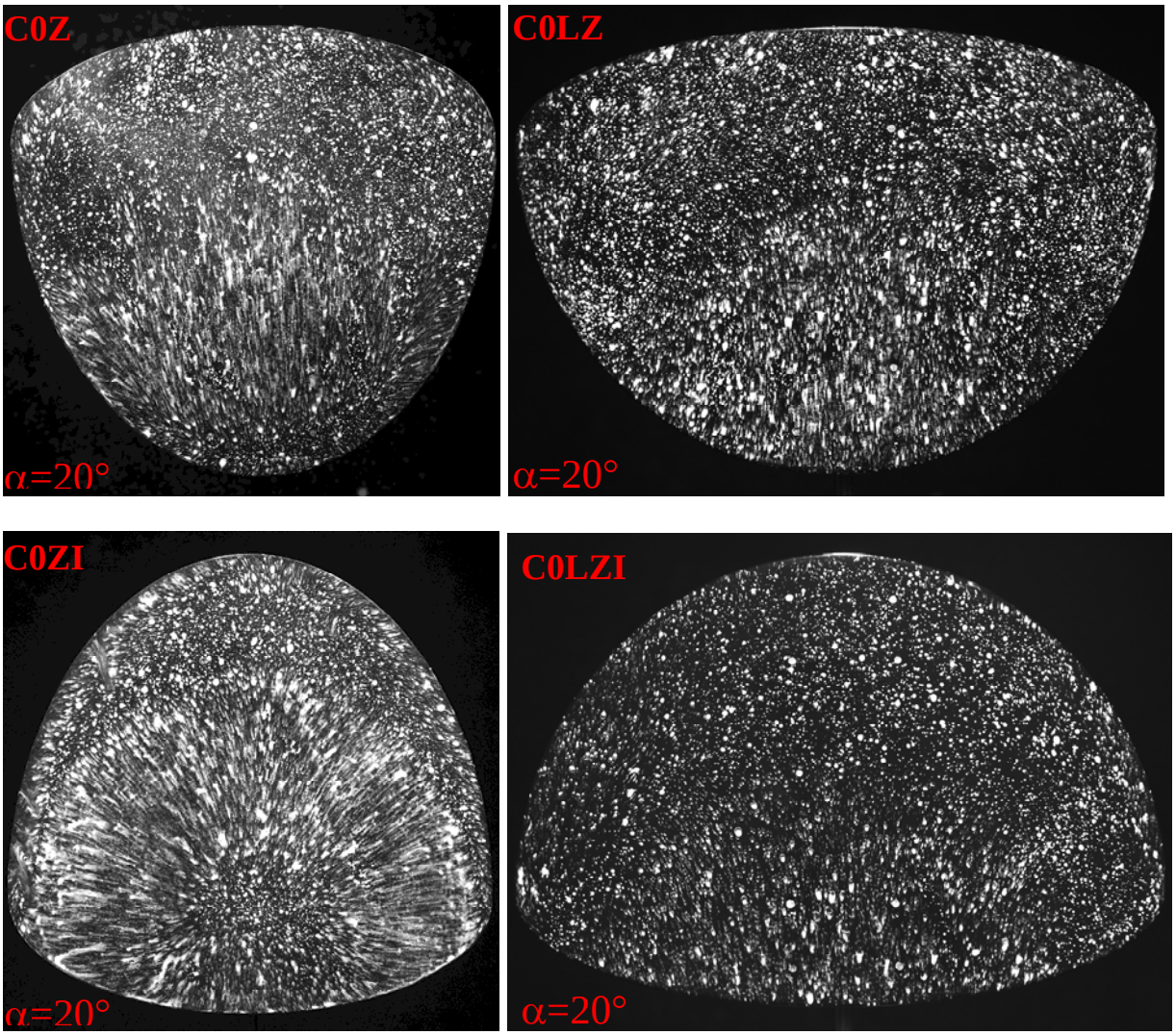

Fig.17 Oil flow visualization photographs comparing normal and larger span planforms C0Z and C0LZ and their inverse C0ZI and C0LZI at α=20°.

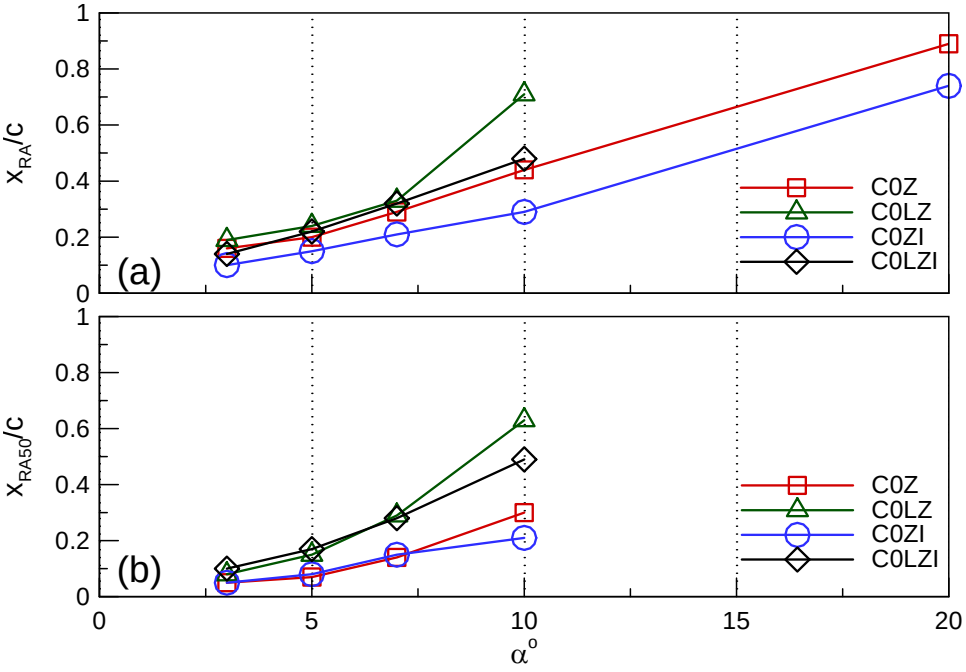

Fig.18 Normalized distance to reattachment from oil flow pictures comparing planforms with normal and larger spans (C0Z and C0LZ) and their inverse (C0ZI and C0LZI)

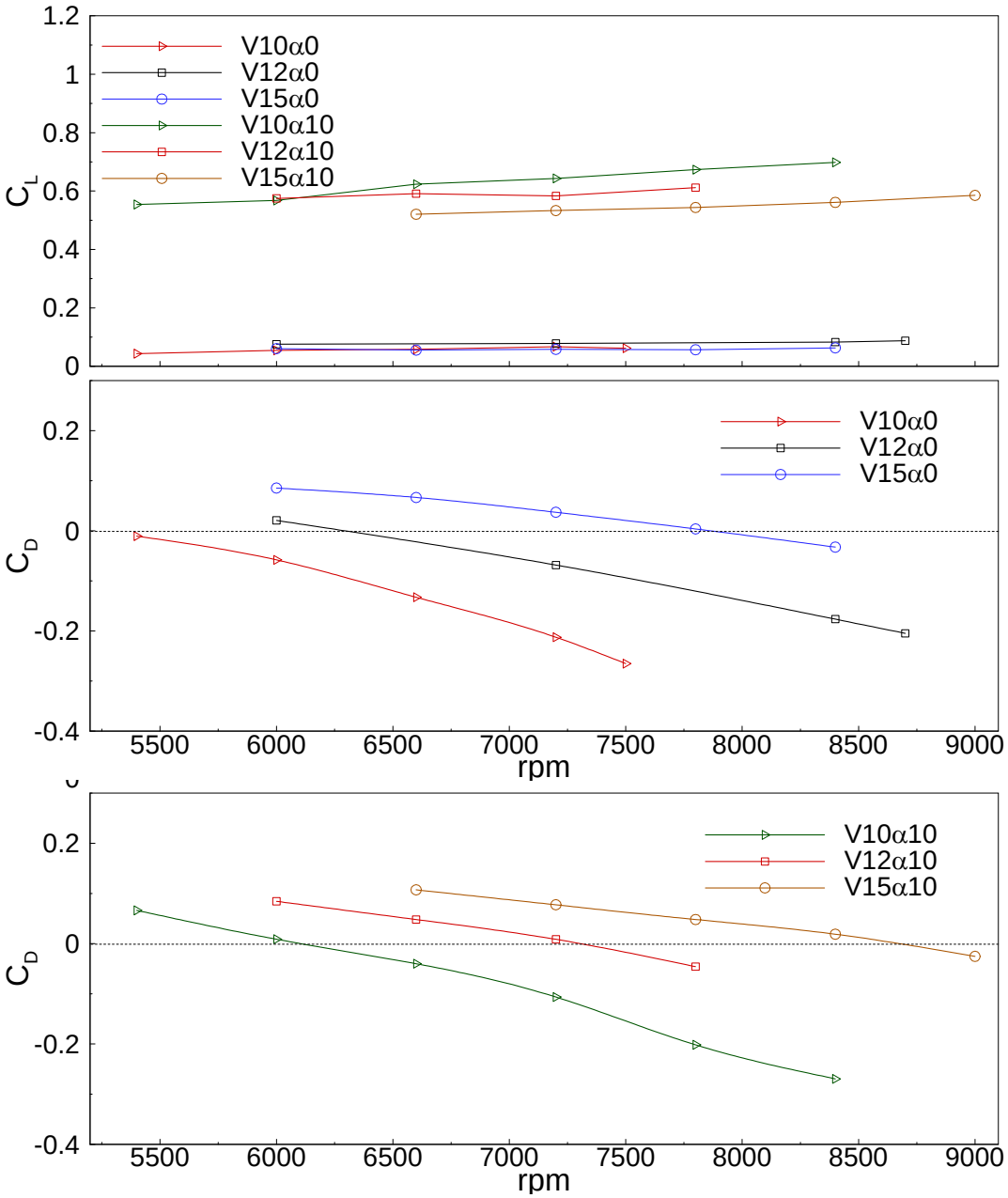

Fig.19 Variation of aerodynamic coefficients with rpm at α=0, 10°

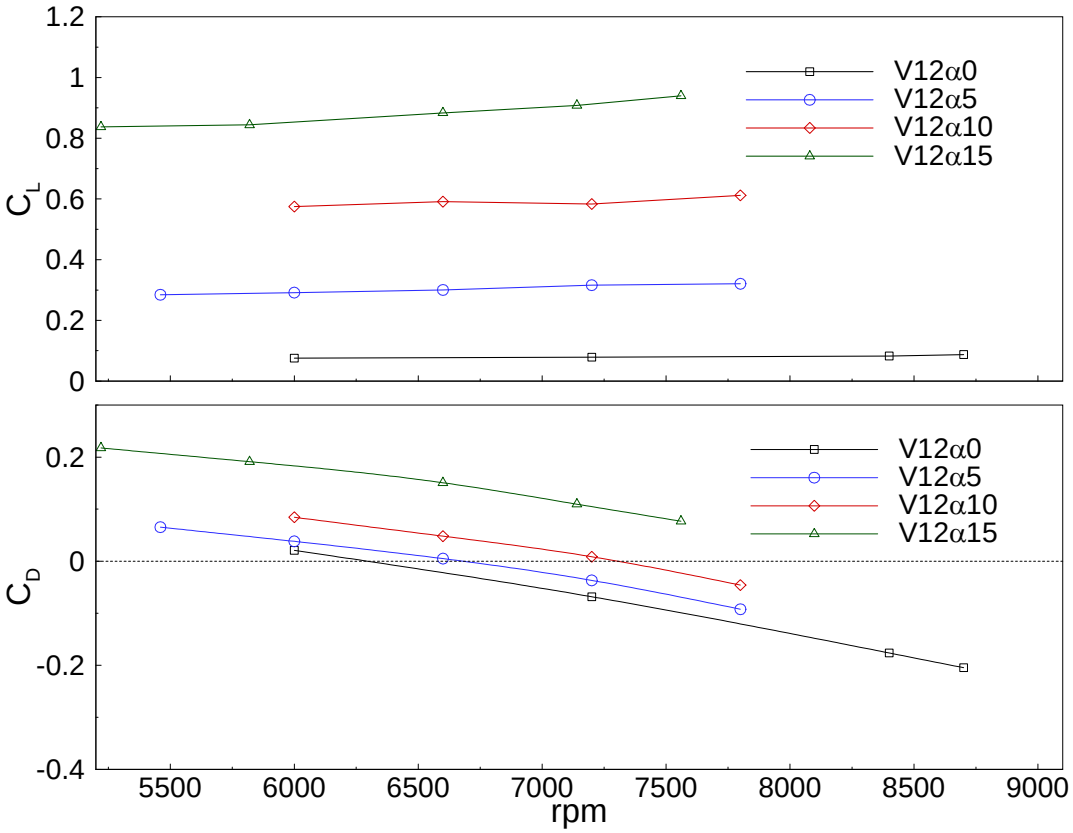

Fig.20 Variation of aerodynamic coefficients at V = 12m/s

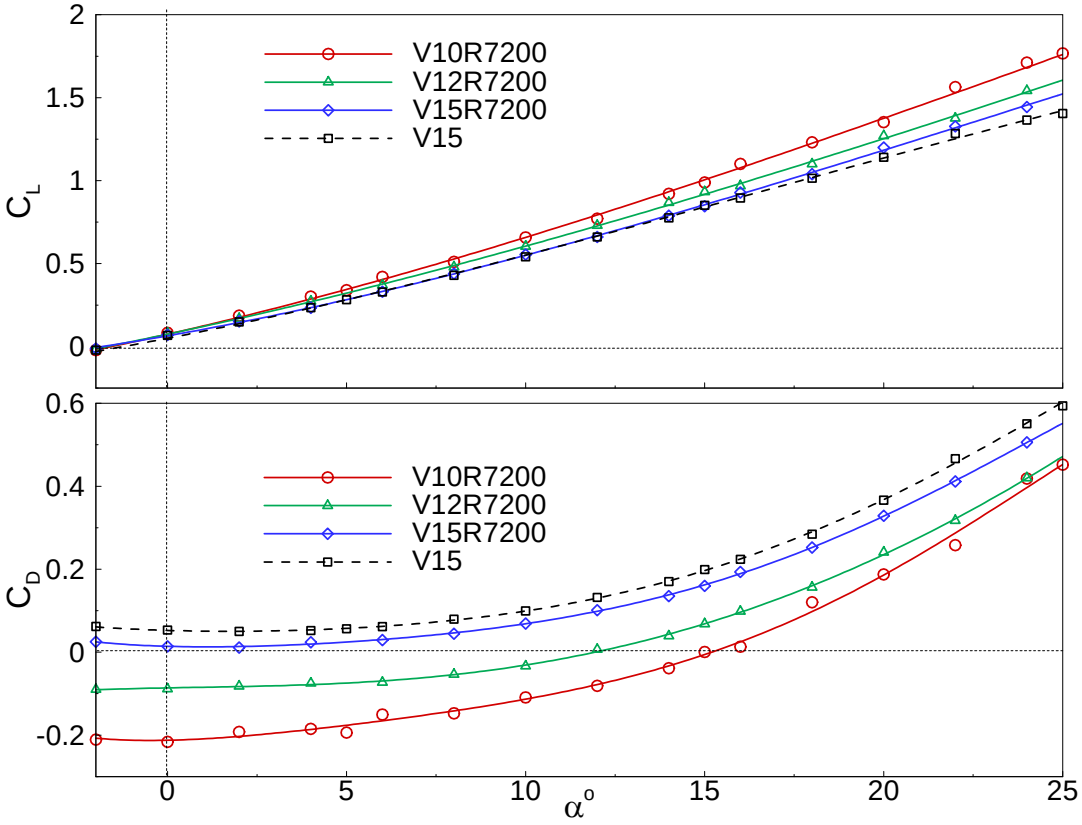

Fig.21 Variation of aerodynamic coefficients with propeller at 7200 rpm

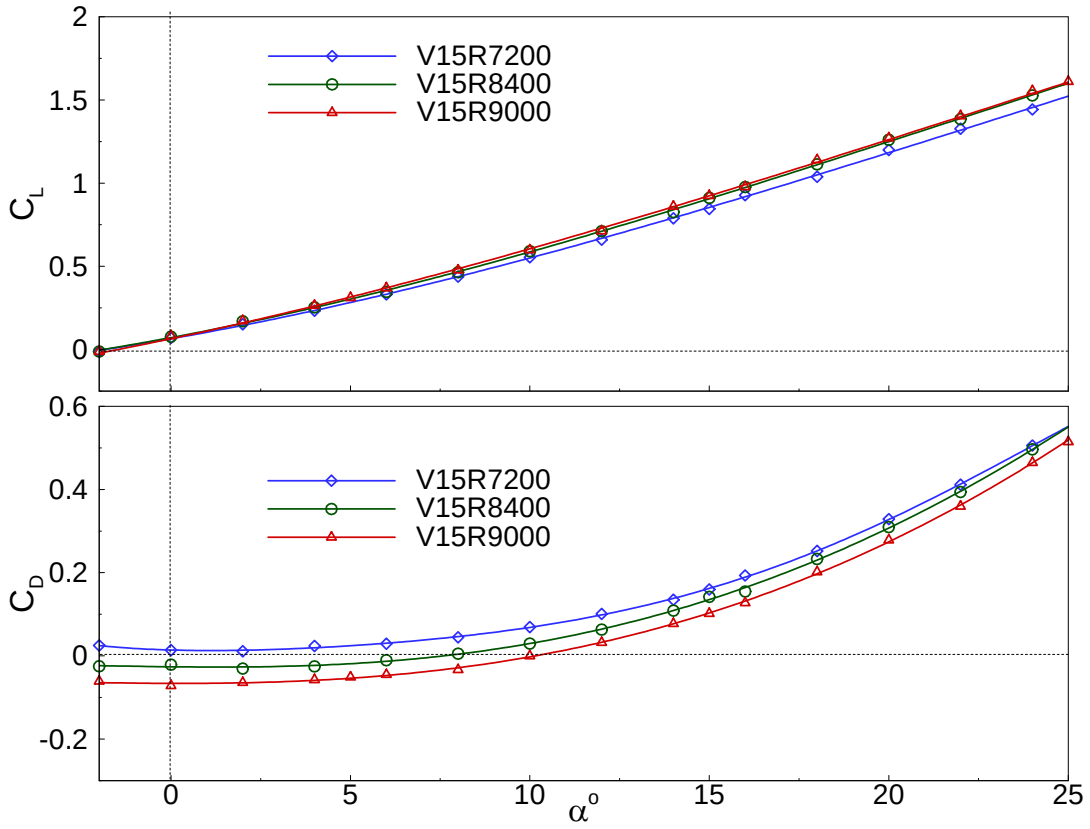

Fig.22 Variation of aerodynamic coefficients at V = 15m/s

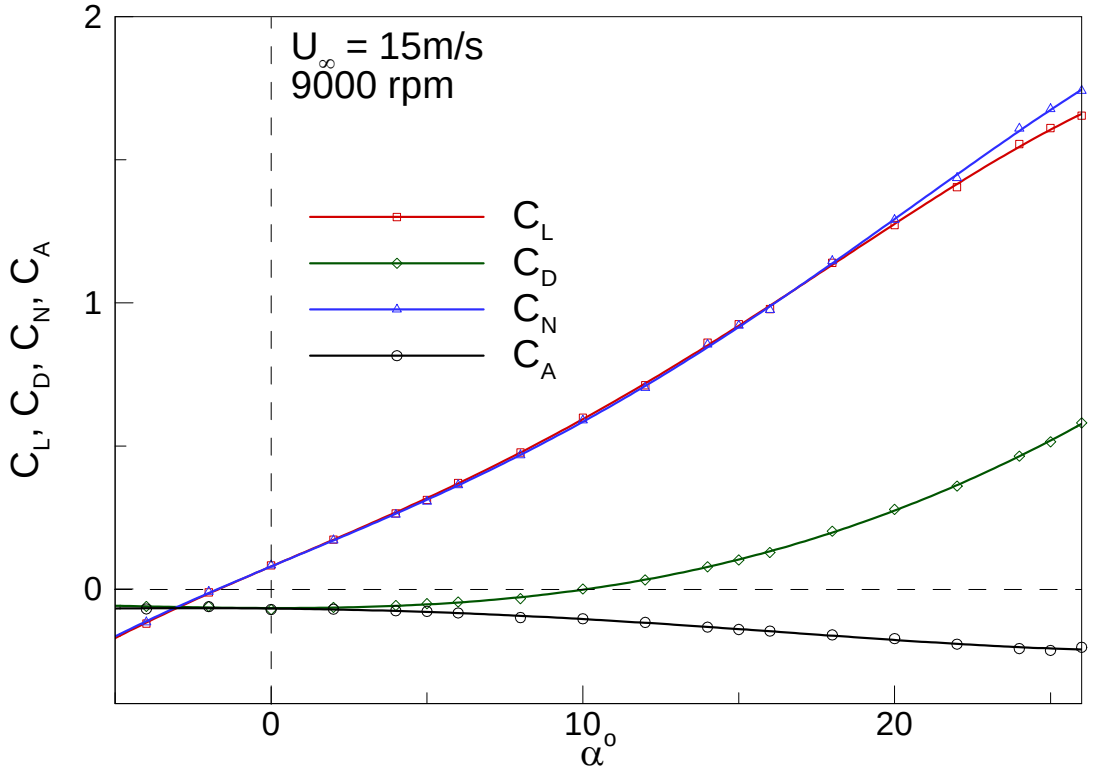

Fig.23 Resolved aerodynamic coefficients of C1MZ at V = 15m/s with propeller

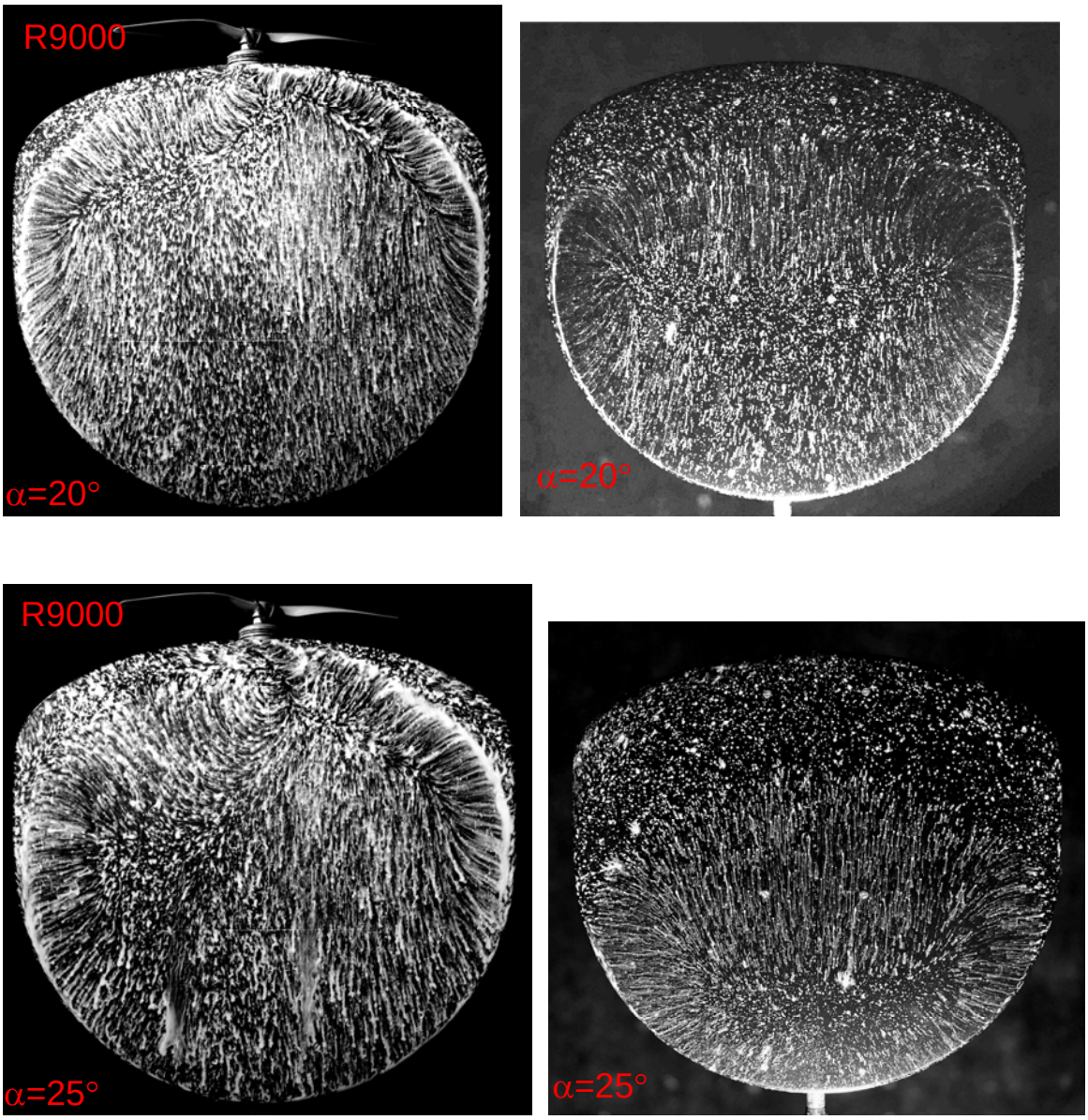

Fig.24 Oil flow over C1MZ with propellers (left) compared to without (right)

DOCUMENTATION SHEET

National Aerospace Laboratories

Class: Unrestricted

No. Copies: 10

Title: Effect of MAV configuration on flow and performance

Authors: Mukund R, Chandan Kumar A

Division: EAD			**Project No:**	
Document No: PD-EAD/2014/1003			**Date of Issue:** August 2014	
Contents:	Pages: 30	Figures: 24	Tables: 3	References: 13

External Participation :

Sponsor :

Approval : Head, EAD

Remarks :

Keywords : MAV, aerodynamic characteristics, propeller

Abstract : Systematic experimental studies were taken up in the 1.5m wind tunnel at NAL on thin constant-thickness MAV planforms to study the effect of a variety of planform configurations on the flow and MAV performance. The first phase was a configuration study over a variety of MAV planform shapes and camber conducting force and pressure measurements along with surface oil flow visualization. In the present second phase, selected planforms were used to study different aspects of the configuration like powered propellers, the leading edge shape and planform aspect ratio. PIV studies on the MAV planform conducted to study the leading edge bubble, the tip vortices and their interactions are reported in the third phase.